Mechanical Systems and Signal Processing 241 (2025) 113445

Contents lists available at ScienceDirect

Mechanical Systems and Signal Processing

journal homepage: www.elsevier.com/locate/ymssp

Full length article

Robust GSR array-assisted fast intelligent diagnosis for multi-harmonic fault characteristics under variable-speed conditions

Xuerui Zhang [a], Xue Wen [a], Lifeng Lin [b], Huiqi Wang [a,*]

[a] College of Mathematics and Statistics, Chongqing University, Chongqing 401331, China
[b] School of Big Data, Fuzhou University of International Studies and Trade, Fuzhou 350202, China

ARTICLE INFO

Communicated by A. Morassi

Dataset link: https://data.mendeley.com/datasets/v43hmbwxpm/2

Keywords:
Intelligent diagnosis
Variable speed conditions
Multi-harmonic fault characteristics (MFCs)
Generalized stochastic resonance (GSR)
Lightweight CNN

ABSTRACT

Bearing vibration signals under variable-speed conditions are highly non-stationary and often contaminated by substantial noise, presenting significant challenges for accurate fault diagnosis. This study proposes a fast intelligent diagnosis method that integrates a generalized stochastic resonance (GSR) array for front-end multi-harmonic fault characteristics (MFCs) enhancement, Markov transition field (MTF) for mid-end MFCs representation, and a lightweight convolutional neural network (CNN) for back-end intelligent classification. First, the first- and second-order stochastic asymptotic stability criterions are introduced to improve the robustness of angular-domain GSR array in enhancing MFCs signal, and a robust fault feature amplification (FFA) index is derived to guide system optimization. The enhanced outputs are then transformed into MTF images in the order spectrum to facilitate MFCs representation. Finally, a lightweight CNN is used to perform intelligent learning and classification, achieving an effective balance between diagnostic accuracy and computational efficiency. Extensive experiments conducted under both original and artificially noise-degraded conditions confirm the efficacy of our approach. On original signals, the approach achieves a mean classification accuracy of 99.69%. Even under severe input signal-to-noise ratio (SNR) degradation exceeding 9 dB, it still achieves a high accuracy of 95.53%, significantly outperforming the compared methods. The extended validation further demonstrates the superiority of parameter transferability, noise resilience, and compound fault identification, indicating considerable potential in addressing the challenges of complex, variable-speed rotating machinery systems.

1. Introduction

As rotating machinery increasingly operates under complex and harsh conditions in industrial applications, bearing failures have become the leading cause of equipment breakdowns, resulting in costly downtime and serious safety risks [1]. Consequently, effective fault diagnosis methods are essential for ensuring system reliability and preventing catastrophic failures. Under constant-speed conditions, numerous approaches have been developed to extract bearing fault features [2,3], including wavelet transform [4], empirical mode decomposition [5], spectral kurtosis [6], and chaos theory [7]. Recently, with the development of resonance theory [8–13], a class of noise-assisted fault diagnosis methods based on the nonlinear SR mechanism has gained considerable attention [14,15]. Extensive research has focused on extending nonlinear structures and implementing adaptive parameter tuning, substantially expanding SR's applicability in mechanical fault diagnosis [16–22].

* Corresponding author.
E-mail address: wanghuiqi@cqu.edu.cn (H. Wang).

https://doi.org/10.1016/j.ymssp.2025.113445
Received 18 May 2025; Received in revised form 5 September 2025; Accepted 28 September 2025
Available online 10 October 2025
0888-3270/© 2025 Published by Elsevier Ltd.

Traditional SR-based methods leverage bistable or multistable systems to transfer energy from additive noise to weak periodic signals, thereby enhancing fault features. It was once believed that nonlinearity, weak periodic excitation, and additive noise were indispensable for SR-based method design. However, subsequent studies have shown that SR-like effects can also emerge in linear systems driven by multiplicative (colored) noise [23–26]. This observation motivated the notion of generalized stochastic resonance (GSR), which emphasizes non-monotonic dependencies of response metrics (e.g., SNR, autocorrelation, and statistical moments) and system or noise parameters. For instance, Chen et al. [27] explored the dynamics of a fluctuating-mass linear oscillator and first proposed a GSR-based bearing fault diagnosis method. Wang et al. [28] analyzed energy conversion mechanisms in fluctuating-frequency oscillators to improve diagnostic performance. Building on these insights, Chen et al. [29] and Zhang et al. [30] proposed diagnosis techniques based on scale-transformed fractional oscillators and fluctuating-damping linear oscillators, respectively. Furthermore, fault feature amplification (FFA) was introduced as an evaluation metric to replace time-consuming numerical optimization, enabling efficient assessment of signal enhancement.

These methods have demonstrated effectiveness under constant-speed conditions. However, in practical industrial settings, equipment often operates under variable-speed conditions, which complicates signal properties and raises the risk of bearing faults. In response, several advanced techniques have been introduced, including computed order tracking (COT) [31], time-varying autoregressive (TVAR) models [32], and angular domain synchronous averaging (ADSA) [33]. Among them, COT is essential for its ability to transform time-domain signals with non-stationary characteristics into stationary angular representations via uniform-angle resampling, thereby mitigating the adverse effects of speed fluctuations. This conversion also broadens the applicability of SR/GSR methods to dynamic-speed diagnostic scenarios. For example, Yang et al. [34] and Wang et al. [35] combined COT with bistable and tri-stable systems, respectively, to propose adaptive frequency-shift SR methods for weak fault detection. Gong et al. [36] further utilized the coupled SR to enhance fault characteristics post-COT transformation.

However, existing SR/GSR-based approaches predominantly simplify vibration signals into idealized sinusoidal forms, focusing on the enhancement of a single fault component. In practice, due to periodic mechanical impacts, real-world bearing signals exhibit complex multi-harmonic fault characteristics (MFCs) [37]. This simplification often results in substantial information loss and compromises diagnostic precision. Therefore, Han et al. [38] introduced a wavelet-driven technique in combination with a parameter-adjusted multistable SR model for detecting MFCs under heavy noise. Shi et al. [39] developed a wavelet multi-scale noise-assisted SR system to detect multi-frequency weak signals in colored noise environments. In recent developments, Qiao et al. [40] involved the use of an SR array structure to enhance weak MFCs for early-stage diagnostics in non-uniform speed environments. Building on this, Zhang et al. [41] combined the GSR array with COT, achieving enhanced detection of weak MFCs through active energy transfer from multiplicative colored noise. However, their results also indicate that in complex diagnostic environments, the GSR array often requires multiple independent trials to ensure stable outcomes, which significantly reduces the diagnostic efficiency. This phenomenon primarily arises from the stochastic regulatory nature of the GSR mechanism, whereby the same sample can exhibit considerable output variability across repeated trials. Nevertheless, the study does not provide a thorough discussion on controlling the stability of the GSR array.

While these methods effectively enhance fault features, they predominantly address signal enhancement and feature extraction, leaving fault identification to subsequent analysis steps such as spectrum interpretation. This post-processing is often subjective, lacks standardized decision criteria, and performs poorly under complex fault patterns or in large-scale data environments [41]. Additionally, industrial environments often involve various interference sources and variable operating conditions. Even after signal enhancement, the fault features may still exhibit strong ambiguity, challenging conventional analysis methods. To overcome these limitations and improve diagnostic automation, researchers have increasingly integrated intelligent diagnostic strategies [42–44]. Among these, deep learning (DL)–especially convolutional neural network (CNN)–has proven highly effective for intelligent fault classification. Furthermore, hybrid frameworks have been proposed, where SR-based signal enhancement serves as the front end, followed by CNN-based classification in the back end. For example, Wang et al. [45] demonstrated that combining multi-parameter optimized SR with CNN significantly improves classification performance under noisy conditions. To exploit CNN's strength in image pattern recognition, various techniques have been proposed to convert 1D vibration signals into 2D images, including traditional time-frequency analysis tools (e.g., continuous wavelet transform (CWT) [46], short-time Fourier transform (STFT) [47]), as well as more recent image-based methods such as Markov transition field (MTF) [48], recurrence plot (RP) [49], and Gramian angular field (GAF) [50]. Liu et al. [51], for instance, applied adaptive SR for noise suppression, converted the enhanced signal into a GAF image, and then performed CNN-based classification, achieving high diagnostic accuracy across varying operating conditions.

Despite these advances, a critical challenge persists: how to effectively address variable-speed conditions and the inherently low-SNR, multi-harmonic characteristics of early bearing fault signals. Furthermore, complex noise environments significantly affect resonance-based enhancement mechanisms [52], further complicating robust fault diagnosis. To tackle these issues, this study proposes a novel and fast intelligent diagnostic framework, RGSRA-MNN, specifically designed for variable-speed conditions. The primary contributions are summarized as follows: (i) We investigate the first- and second-order stochastic asymptotic stabilities of an angular-domain GSR array and propose a robust FFA index to guide system optimization within constraint stability conditions. (ii) We extend the MTF-based feature representations by transforming the MFCs order spectrum into structured and discriminative MTF images, which supports more reliable classification in complex fault scenarios. (iii) We develop a fast intelligent diagnostic framework, RGSRA-MNN, comprising three key components: a robust GSR array for MFCs enhancement (front-end), MTF-based MFCs representation (mid-end), and a lightweight CNN for intelligent learning and classification (back-end). This design achieves a balance between diagnostic accuracy and computational efficiency, offering a practical solution for more complex and data-intensive industrial fault diagnosis tasks.

The remainder of this paper is organized as follows: Section 2 details the robust GSR array model. Section 3 introduces the proposed intelligent diagnostic framework. Section 4 presents experimental validation. Finally, conclusions are drawn in Section 5.

2. Robust GSR array for MFCs enhancement

2.1. GSR array in angular domain

In rotating machinery, bearing faults typically manifest as periodic impacts induced by mechanical rotation. These impacts generate not only the fundamental fault frequency but also its harmonics, resulting in fault signals characterized by complex MFCs. Relying on a single fault feature often leads to significant information loss and diminished diagnostic accuracy. This challenge is further compounded under speed fluctuations, where the fault characteristic frequencies shift continuously over time, causing spectral smearing that undermines conventional frequency-domain analysis. To address the complications, non-stationary signals are resampled into the angular domain, resulting in more stable signal representations [31]. Building on this, we extend our investigation into the angular domain, focusing on the enhancement and diagnosis of weak MFCs using a GSR array.

Specifically, we consider an angular-domain bearing fault signal $s_{\mathrm{v}}(\theta)$, exhibiting weak MFCs at orders $\mu_1,\ \mu_2, \ldots, \mu_m$. This signal can be decomposed into a series of harmonic components [53,54]: $s_k(\theta) = c_k \sin(2\pi\mu_k\theta + \varphi_k)$ for $k = 1, 2, \ldots, m$, where c_k and φ_k denote the amplitude and phase of the kth fault component, respectively. Motivated by this observation, we construct a GSR array comprising m angular-domain linear oscillators with stochastically modulated damping, aiming to jointly enhance the weak MFCs. The system dynamics are governed by

$$\ddot{\mathbf{x}}(\theta) + \mathbf{R}\boldsymbol{\Gamma}\left[\mathbf{E} + \boldsymbol{\Xi}(\theta)\right]\dot{\mathbf{x}}(\theta) + \mathbf{R}^2\boldsymbol{\Omega}^2\mathbf{x}(\theta) = \mathbf{R}^2\mathbf{g}(\theta), \tag{1}$$

where

- $\mathbf{g}(\theta) = [g_1(\theta), g_2(\theta), \ldots, g_m(\theta)]^{\top}$ denotes the input signals to the oscillator array, each defined as $g_k(\theta) = s_k(\theta) + \eta(\theta)$ including a weak fault component $s_k(\theta)$ embedded in additive noise $\eta(\theta)$; $\mathbf{x}(\theta) = [x_1(\theta), x_2(\theta), \ldots, x_m(\theta)]^{\top}$ represents the system outputs.
- $\boldsymbol{\Gamma} = \mathrm{diag}\{\gamma_1, \ldots, \gamma_m\}$, $\boldsymbol{\Omega} = \mathrm{diag}\{\omega_1, \ldots, \omega_m\}$, and $\mathbf{R} = \mathrm{diag}\{R_1, \ldots, R_m\}$ are diagonal coefficient matrices. Here γ_k, ω_k, and R_k represent the damping coefficient, natural frequency, and generalized scaled transformation (GST) tuning coefficient, respectively, with R_k controlling each oscillator to generate high-frequency GSR for enhanced fault component included in $g_k(\theta)$ [55,56];
- $\boldsymbol{\Xi}(\theta) = \mathrm{diag}\{\xi_1(\theta), \xi_2(\theta), \ldots, \xi_m(\theta)\}$ introduces stochastic regulation, utilizing binary i.i.d. processes $\xi_k(\theta) \in \{-\sigma_k, \sigma_k\}$ that satisfy $\langle \xi_k(\theta) \rangle = 0$. The correlation function is given by $\langle \xi_k(\theta)\xi_l(\theta') \rangle = \sigma_k\sigma_l\delta_{kl}\ \mathrm{e}^{-R_k\lambda_k|\theta-\theta'|}$, where σ_k^2 and $R_k\lambda_k$ represent the regulation intensity and switching rate, respectively. The regulation ensures $1 + \xi_k(\theta) > 0$ preserving physical feasibility. Recent research has revealed that such damping effects may generate diverse resonant behaviors [57–60].
- $\eta(\theta)$ is the background noise, modeled as white Gaussian noise (WGN), such that $\langle \eta(\theta) \rangle = 0$, and $\langle \eta(\theta)\eta(\theta') \rangle = 2D\delta(\theta - \theta')$, with D denoting noise intensity. It is assumed to be uncorrelated with $\xi_k(\theta)$: $\langle \eta(\theta)\xi_k(\theta') \rangle = 0$.

All oscillators in the GSR array are characterized by similar mathematical structures, we analyze the system steady-state responses [8], and derive their asymptotic expressions for the first-order moment of oscillator outputs:

$$\langle x_k(\theta) \rangle_{\mathrm{as}} = \langle x_k(\theta) \rangle\big|_{\theta\to\infty} = A_k \sin\left(2\pi\mu_k\theta + \psi_k\right), \quad k = 1, 2, \ldots, m, \tag{2}$$

where A_k and ψ_k denote the enhanced amplitude and phase shift, with their explicit expressions provided in Appendix A. Based on the Routh–Hurwitz criterion [61,62], the derivation is valid only if the system parameters satisfy the *first-order stochastic asymptotic stability condition* in Eq. (A.6). This specifies a feasible parameter space $\mathcal{P}_k^{1\mathrm{st}}$, whose complete expression is also provided in this Appendix. Through straightforward verification, it can be shown that the GSR array naturally satisfies this condition when $\sigma_k \in (0, 1)$.

To quantify the enhancement of MFCs at $\mu_1, \mu_2, \ldots, \mu_m$, we define the fault feature amplification (FFA) index:

$$G(\mathbf{p}_k|\mu_k) = R_k^2\sqrt{\frac{m_1^2 + m_2^2}{m_3^2 + m_4^2}}. \tag{3}$$

Hence, the optimal GSR array design can be achieved by maximizing the theoretical FFA index $G(\mathbf{p}_k|\mu_k)$ for each $k = 1, 2, \ldots, m$.

2.2. Robust GSR array

The first-order stochastic asymptotic stability condition guarantees the asymptotic stability of each oscillator's mean output under random regulation $\xi_k(\theta)$. However, this condition alone is insufficient to meet practical requirements for efficient and rapid fault diagnosis [63,64]. To ensure the reliability of individual diagnostic outcomes — beyond statistical averages — it is necessary to consider second-order stochastic asymptotic stability.

We further apply the Routh–Hurwitz criterion to define the parameter space constraints $\mathcal{P}_k^{2\mathrm{nd}}$ that ensure second-order stochastic asymptotic stability, specifically the asymptotic stability of the second moment $\langle x_k^2(\theta) \rangle$ for $k = 1, 2, \ldots, m$. Moreover, by restricting the system parameters $\mathbf{p}_k = [\gamma_k, \omega_k, \sigma_k, \lambda_k, R_k]$ to the intersection $\mathcal{P}_k^{1\mathrm{st}} \cap \mathcal{P}_k^{2\mathrm{nd}}$, the asymptotic stability of both the first and second moments of all system outputs $x_k(\theta)$, $k = 1, 2, \ldots, m$, is ensured, thereby reducing output variance and enhancing diagnostic reliability. The complete mathematical formulations, coefficient specifications, and detailed derivations have been provided in Appendix B. For simplicity in the derivation, the subscript k in all parameter expressions (i.e., $\mathbf{p}_k = [\gamma_k, \omega_k, \sigma_k, \lambda_k, R_k]$ and the fault order μ_k) has been omitted.

Accordingly, we define the GSR array system that satisfies both first- and second-order stability conditions as the *robust GSR array*:

$$\begin{cases} \ddot{\mathbf{x}}(\theta) + \mathbf{R}\boldsymbol{\Gamma}\left[\mathbf{E} + \boldsymbol{\Xi}(\theta)\right]\dot{\mathbf{x}}(\theta) + \mathbf{R}^2\boldsymbol{\Omega}^2\mathbf{x}(\theta) = \mathbf{R}^2\mathbf{g}(\theta), \\ \text{s.t. } \mathbf{p}_k \in \mathcal{P}_k^{1\text{st}} \cap \mathcal{P}_k^{2\text{nd}},\ k = 1, 2, \ldots, m. \end{cases} \tag{4}$$

To evaluate the practical significance of these stability conditions and to demonstrate the advantages of the robust GSR array, we conduct a relative error analysis to quantify the discrepancy between the theoretical asymptotic response and the actual system outputs in the angular domain. Two comparative cases are considered: (i) GSR array: satisfying only first-order stochastic asymptotic stability condition, i.e., $\mathbf{p}_k \in \mathcal{P}_k^{1\text{st}} \setminus \mathcal{P}_k^{2\text{nd}}$; (ii) Robust GSR array: satisfying both first- and second-order stability conditions, i.e., $\mathbf{p}_k \in \mathcal{P}_k^{1\text{st}} \cap \mathcal{P}_k^{2\text{nd}}$. An example of the system input $g(\theta)$, composed of three harmonic signals embedded in heavy background noise, is shown in Fig. 1(a). The output results for the GSR array are presented in Fig. 1(b1) and (b2). Notably, the red curve in Fig. 1(b1) represents the mean output over 100 trials, while individual outputs exhibit pronounced fluctuations around this average. As shown in Fig. 1(b2), the relative error decreases with increased averaging but remains above 0.2 even after 100 repetitions. This highlights the inherent limitation of conventional GSR arrays that rely solely on first-order stochastic asymptotic stability, resulting in substantial output variability. In comparison, Fig. 1(c1) and (c2) present the results for the robust GSR array. In Fig. 1(c1), individual outputs almost coincide with the average output (red curve), exhibiting only minor amplitude fluctuations. As illustrated in Fig. 1(c2), the relative error falls below 0.2 after a single trial and continues to decrease with further averaging. These results confirm that, by incorporating second-order stochastic asymptotic stability, the robust GSR array achieves significantly improved output consistency.

Building on these findings, the robust GSR array design substantially enhances diagnostic efficiency and reliability, contributing to the theoretical development of high-performance fault diagnostic strategies. Its optimal configuration can thus be systematically determined by maximizing the theoretical FFA index $G(\mathbf{p}_k|\mu_k)$ within the rigorously defined admissible parameter space $\mathbf{p}_k \in \mathcal{P}_k^{1\text{st}} \cap \mathcal{P}_k^{2\text{nd}}$ for each $k = 1, 2, \ldots, m$.

3. Fast intelligent diagnosis framework: RGSRA-MNN

3.1. MTF representation based on angular-domain order spectrum

To leverage CNN's strength in image recognition, extensive research has transformed 1D vibration signals into 2D image representations, which more comprehensively capture the dynamic characteristics of fault signals across both time and frequency domains [65].

Building upon this concept, we extend the application of MTF representation to the order spectrum of MFCs. Specifically, we begin by performing FFT on the GSR array-enhanced signals to extract their order spectra. We then concentrate on spectral components in the vicinity of fault-related orders and define a frequency band $[\mu_{\min}, \mu_{\max}]$ that encompasses each target fault order μ_k, $k = 1, 2, \ldots, m$, to retain all critical fault-related spectral information. Next, we truncate the order spectrum within this band to obtain an amplitude sequence $y_1, y_2, \ldots, y_n$, where y_1 and y_n represent the amplitudes at $\mu_{\min}$ and $\mu_{\max}$, respectively. This sequence is then symbolized by mapping each value y_i into one of Q quantile bins r_j, $j = 1, 2, \ldots, Q$. By calculating the transition probabilities between adjacent quantile bins in this sequence, we construct an $Q \times Q$ Markov transition probability matrix $\mathbf{W} = (w_{ij})_{Q\times Q}$, where $w_{ij} = P\{y_{t+1} \in r_i \mid y_t \in r_j\}$ represents the transition probability from bin r_j at time t to bin r_i at time $t+1$. Subsequently, based on the transition probability matrix, we generate the MTF matrix $\mathbf{M}$ of size $n \times n$, capturing the global state transition dynamics throughout the entire amplitude sequence:

$$\mathbf{M} = \begin{pmatrix} m_{ij} \mid y_1 \in r_i, y_1 \in r_j & \cdots & m_{ij} \mid y_1 \in r_i, y_n \in r_j \\ m_{ij} \mid y_2 \in r_i, y_1 \in r_j & \cdots & m_{ij} \mid y_2 \in r_i, y_n \in r_j \\ \vdots & \ddots & \vdots \\ m_{ij} \mid y_n \in r_i, y_1 \in r_j & \cdots & m_{ij} \mid y_n \in r_i, y_n \in r_j \end{pmatrix}, \tag{5}$$

where m_{ij} denotes the transition probability from quantile bin r_j to r_i.

Compared with conventional time- or angular-domain MTF representations, the proposed order spectrum-based MTF framework provides clearer insights into the relationships among fault information. This enhancement enables DL models to extract more discriminative features, thereby significantly improving the identification accuracy.

3.2. Lightweight CNN classifier

Although MTF images effectively capture the order spectrum characteristics enhanced by the robust GSR array, accurately distinguishing fault categories based solely on visual inspection remains challenging in practical applications. Thus, we further design a lightweight CNN for intelligent feature learning and classification. The proposed CNN consists of two convolutional layers, two pooling layers, and two fully connected layers. The corresponding hyperparameter configurations are listed in Table 1, and the network architecture is depicted in Fig. 2. The convolutional operation performs hierarchical feature extraction and can be expressed as

$$z_s^{(l)} = f\left(\sum_{j=1}^{J} w_{js}^{(l)} * z_j^{(l-1)} + B_s^{(l)}\right), \tag{6}$$

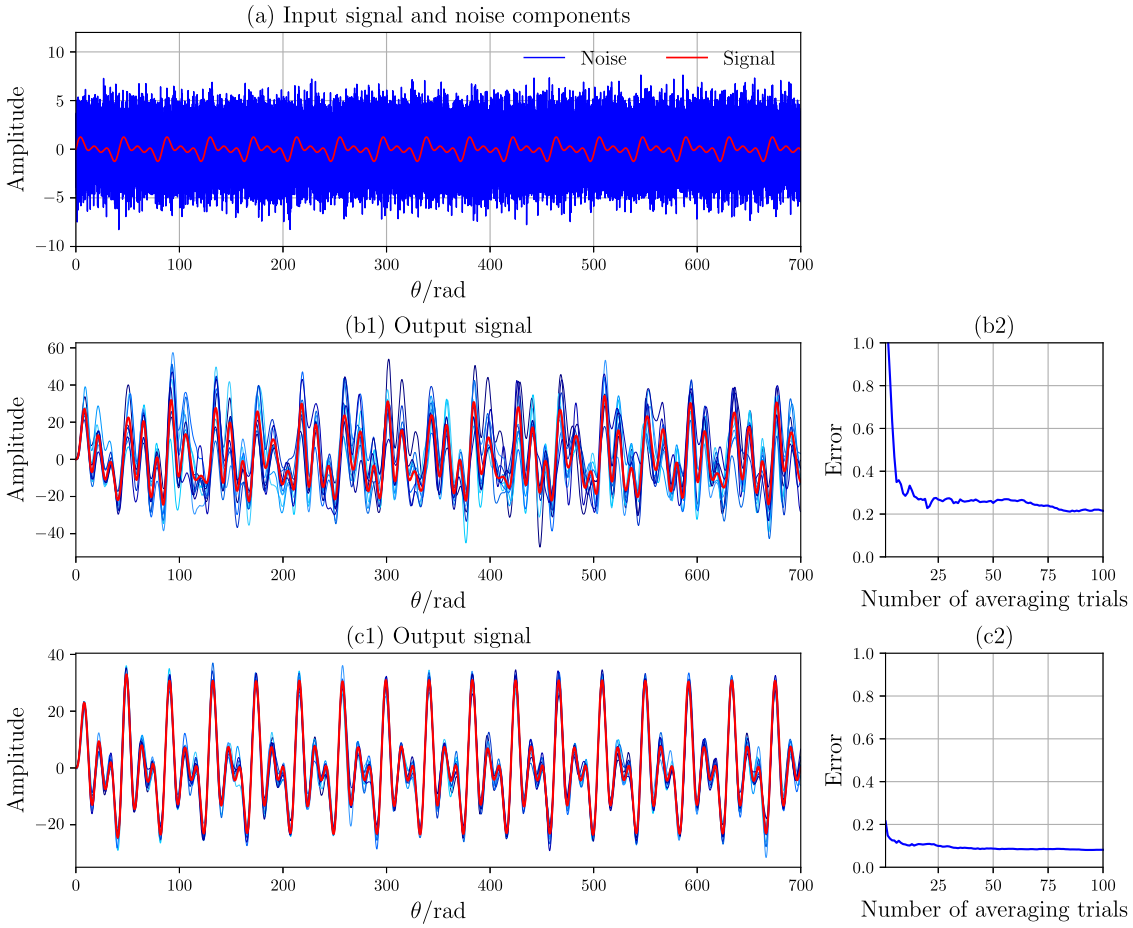

Fig. 1. The influence of stochastic asymptotic stability on the system outputs: (a) system input $g(\theta) = A_0 \sum_{k=1}^{3} \sin(2\pi\mu_k\theta)$ with $A_0 = 0.5$, $\mu_k = k \times 4.31$, $D = 2$; (b1)–(b2) system outputs of GSR array (repeat 10 times), with parameters: $\mathbf{p}_1 = [1, 0.26, 0.96, 0.25, 173.08]$, $\mathbf{p}_2 = [0.04, 0.39, 0.18, 76.93, 189.65]$, $\mathbf{p}_3 = [0.001, 0.64, 0.94, 10.06, 151.22]$; (c1)–(c2) system outputs of robust GSR array (repeat 10 times), with parameters: $\mathbf{p}_1 = [1, 1.56, 0.58, 78.82, 21.67]$, $\mathbf{p}_2 = [0.10, 0.34, 0.01, 89.22, 199.61]$, $\mathbf{p}_3 = [0.08, 0.48, 0.10, 1.03, 185.67]$. (For interpretation of the references to color in this figure legend, the reader is referred to the web version of this article.)

Table 1
The implementation details of the lightweight CNN.

Hyperparameter	Value	Hyperparameter	Value
Number of convolutional layer	2	Initial learning rate	0.001
Number of pooling layer	1	Dropout rate	0.3
Number of fully connected layer	2	Stride	2
Batch size	32	Padding	1
Kernel size	3 × 3	Optimizer	Adam
Pooling size	2 × 2	Epochs	100

where $z_s^{(l)}$ denotes the sth feature map of the lth layer; $w_{js}^{(l)}$ is the convolution kernel weight connecting the jth input to the sth output; $z_j^{(l-1)}$ is the jth feature map from the previous layer; $B_s^{(l)}$ is the bias term for the sth feature map; and $f(\cdot)$ is the activation function. In this study, we adopt the Rectified Linear Unit (ReLU) as the activation function, defined as

$$u_{ijk}^{(l)} = \max\left\{0, z_{ijk}^{(l)}\right\}, \tag{7}$$

where $u_{ijk}^{(l)}$ represents the output at position (i, j) on the kth feature map in the lth layer.

To reduce the dimensionality of convolutional output and mitigate overfitting, a max-pooling layer is applied. The max-pooling operation is formulated as

$$p_{ijk}^{(l)} = \max_{(i',j')\in\mathcal{R}_{ij}} u_{i'j'k}^{(l-1)}, \quad 1 \le i' \le N,\ 1 \le j' \le K,\ i', j' \in \mathbb{Z}^+, \tag{8}$$

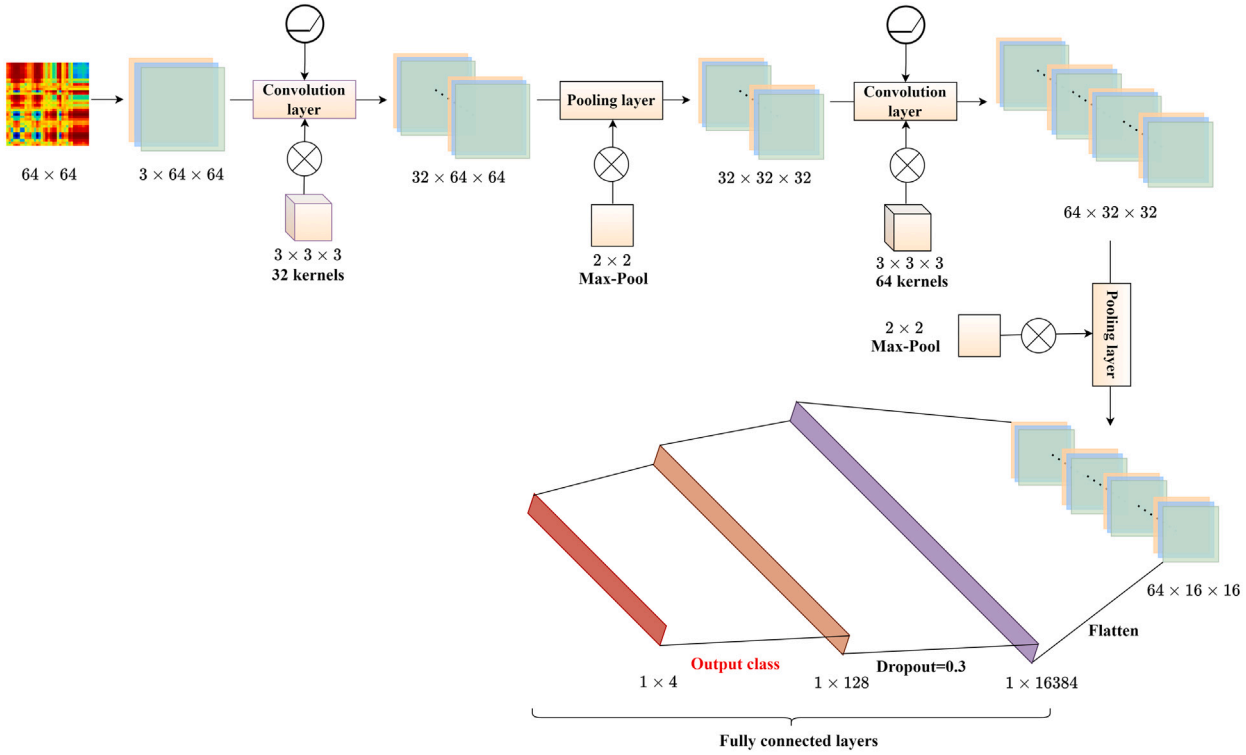

Fig. 2. Lightweight CNN architecture.

where $p_{ijk}^{(l)}$ denotes the pooled output at (i, j) on the kth feature map, derived from input values $u_{i'j'k}^{(l-1)}$ within the window $\mathcal{R}_{ij}$; the pooling window dimensions are $N \times K$.

The final classification results are derived by fully connected layers, which consolidate high-level representations from earlier stages. The operation is defined as

$$\mathbf{U}^{(l)} = f\left(\mathbf{W}^{(l)}\mathbf{Z}^{(l-1)} + \mathbf{b}^{(l)}\right), \tag{9}$$

where $\mathbf{U}^{(l)}$ is the output vector of the lth fully connected layer; $\mathbf{W}^{(l)}$ is the weight matrix; $\mathbf{Z}^{(l-1)}$ is the input from preceding layer; and $\mathbf{b}^{(l)}$ is the corresponding bias vector.

3.3. Fast intelligent diagnostic flowchart

We outline the proposed fast intelligent diagnostic framework in Fig. 3, which consists of the following three main stages:

- **Step 1: Front-end MFCs enhancement.** In this stage, quantum particle swarm optimization is integrated into the robust GSR array configuration [66] to enhance MFCs embedded in complex signals by maximizing the FFA for each fault order μ_k within the admissible parameter space $\mathbf{p}_k \in \mathcal{P}_k^{1\text{st}} \cap \mathcal{P}_k^{2\text{nd}}$, $k = 1, 2, \ldots, m$. Here, the vibration signal is resampled via the COT method to convert them into angular-domain representation. The resampled signals are subsequently processed through the optimal robust GSR array to obtain the summation of outputs after the angular-domain enhancement of MFCs.
- **Step 2: Mid-end MTF-based signal visualization.** In this stage, the enhanced signals are transformed into MTF images to facilitate visual learning. First, the summation of optimal outputs is converted into its order spectra via FFT. Then, only the spectral components within a specified range $[\mu_{\min}, \mu_{\max}]$ are retained to highlight critical fault features. The truncated spectra are discretized into Q quantization bins, based on which 2D MTF images are constructed. These images serve as highly discriminative inputs for subsequent fault recognition and classification tasks.
- **Step 3: Back-end intelligent diagnosis via lightweight CNN.** In the final stage, a lightweight CNN is used to perform automatic fault identification and classification based on the generated MTF images. The dataset is randomly partitioned into training and testing subsets. This CNN model is trained via backpropagation using the training set, and its diagnostic performance is evaluated on the test set by comparing predicted labels against ground truth.

In the optimization process of robust GSR array, the theoretical FFA index $G(\mathbf{p}_k|\mu_k)$ is adopted as the objective function for each $k = 1, 2, \ldots, m$ within the QPSO algorithm. The exact fault characteristic orders μ_k are typically unknown in practice. Instead, approximate values $\hat{\mu}_k$ can be readily estimated from the equipment's operating conditions using kinematic relationships [1].

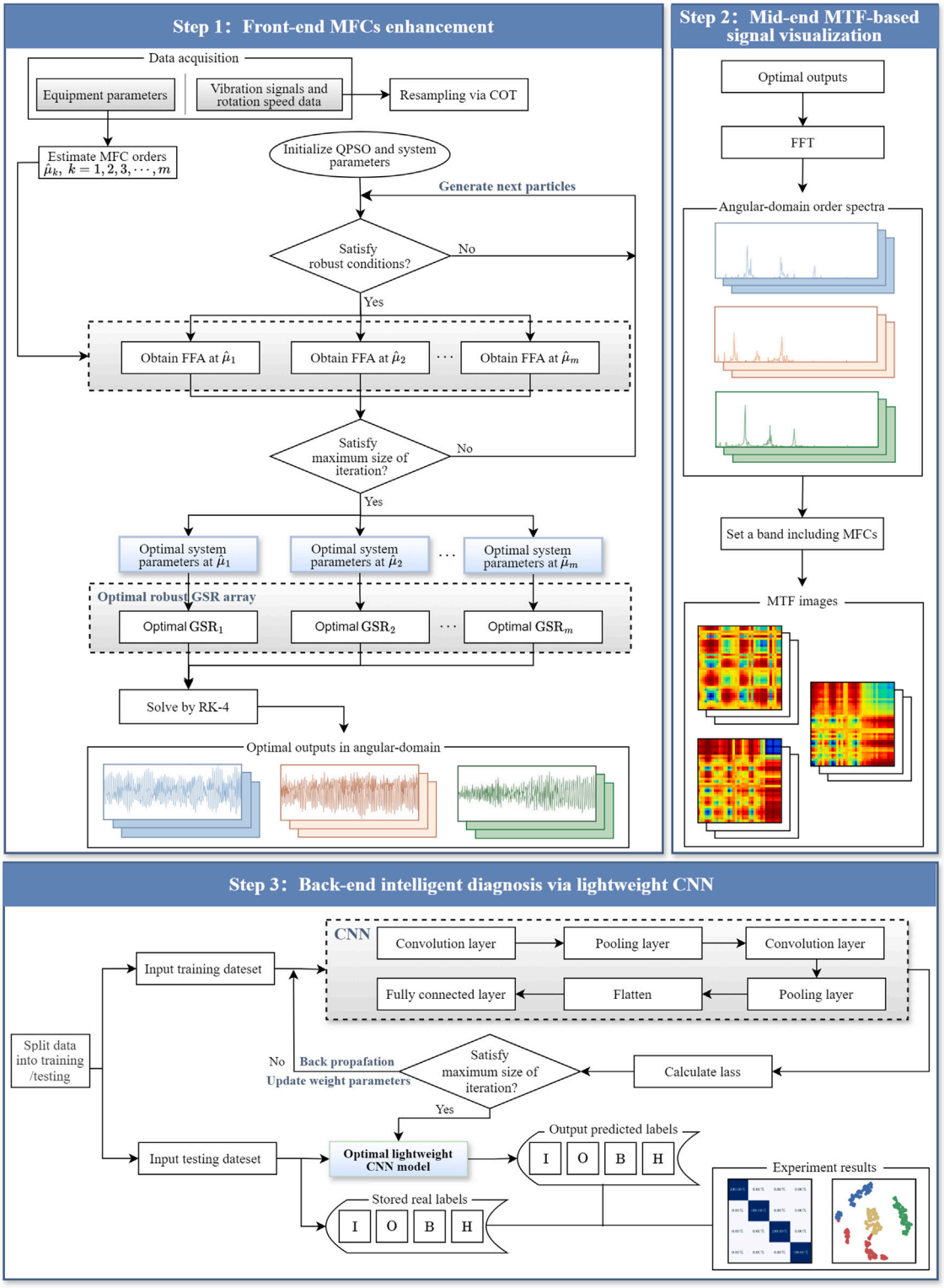

Fig. 3. The fast intelligent diagnostic flowchart.

Accordingly, the optimization problem is reformulated as

$$\mathbf{p}_k^{\text{opt}} = \arg \max_{\mathcal{P}_k^{1\text{st}} \cap \mathcal{P}_k^{2\text{nd}}} G(\mathbf{p}_k \mid \hat{\mu}_k), \quad k = 1, 2, \ldots, m. \tag{10}$$

For each $k = 1, 2, \ldots, m$, the global search domain $\mathcal{P}$ spans predefined intervals for each model parameter, specifically: $\mathbf{p}_k \in [0.001, 2] \times [0.1, 2] \times [0.01, 0.99] \times [0.1, 100] \times [1, 200]$ for $k = 1, 2, \ldots, m$.

Evidently, the optimization is guided by the theoretical FFA index $G(\mathbf{p}_k|\hat{\mu}_k)$, which only requires the prior information $\hat{\mu}$. This value remains constant under fixed equipment parameters and does not vary with the equipment's real-time operating conditions. As a result, there is no need to re-optimize the parameters for each sample, effectively eliminating repeated executions of the QPSO algorithm. This greatly reduces the computational burden of real-time multi-parameter optimization and significantly improves diagnostic efficiency. Furthermore, to ensure numerical stability and accuracy, the classical fourth-order Runge–Kutta (RK-4) method is employed to numerically solve the robust GSR array in Eq. (4).

4. Experimental verification

In this section, all experiments are conducted on an Intel Core Ultra 9 275HX processor and an NVIDIA RTX 5060 GPU with 8 GB of VRAM, and implemented using Python 3.11.3 with PyTorch 2.7.1.

4.1. Experimental description

4.1.1. Datasets

In the experiments, the datasets employed were obtained from University of Ottawa, and were acquired using the SpectraQuest machinery fault simulator (MFS-PK5M) [67]. Vibration and rotation speed data were simultaneously acquired using NI USB-6212 BNC boards, with the bearing type ER16K configured for different conditions.

We examined four types of bearing vibration signals representing various operating conditions, including both healthy and faulty states under accelerating and decelerating speed profiles. Specifically, these datasets include: (i) I-A-3: inner race fault signal during acceleration, (ii) O-B-1: outer race fault signal during deceleration, (iii) B-A-1: rolling element fault signal during acceleration, (iv) H-B-1: healthy signal during deceleration. All signals were sampled at 20 kHz over a 10-second (s) interval. The raw vibration signals and associated speed profiles for each scenario are illustrated in Fig. 4. Based on kinematic equations [1], the theoretical fault characteristic orders were calculated as follows: $\hat{\mu}_{\text{i}} = 5.43$ for inner race faults, $\hat{\mu}_{\text{o}} = 3.57$ for outer race faults, and $2\hat{\mu}_{\text{b}} = 4.31$ for the even harmonics of rolling element faults. Accordingly, The orders involved in the joint diagnosis based on MFCs are configured as $k \times \hat{\mu}_{\text{i}}$, $k \times \hat{\mu}_{\text{o}}$, $k \times 2\hat{\mu}_{\text{b}}$ for $k = 1, 2, 3$, respectively.

Intelligent diagnosis methods typically require large-scale datasets to perform effectively. To meet this demand, we applied a sliding window segmentation strategy. Each window captures 1 s of signal data, and successive windows are shifted by 0.015 s to create overlapping samples. This approach expanded each dataset to 600 samples. Subsequently, the data were randomly partitioned into training and testing sets using a 7:3 ratio, ensuring a representative and balanced evaluation of model performance.

4.1.2. Comparison methods

To thoroughly validate the diagnostic capability of the proposed RGSRA-MNN, we performed comparative experiments against five baseline methods, all of which adopt the same lightweight CNN back-end while differing in their front-end signal enhancement approaches:

- **MNN**: Converts the order spectra of COT-processed raw signals directly into MTF images, omitting any front-end enhancement.
- **EMNN**: Extends MNN by incorporating envelope analysis. The angular-domain envelope signals are extracted, transformed into the order spectra, and then converted into MTF images, still without specialized enhancement.
- **OBSR-MNN**: Applies an overdamped bistable SR system for front-end enhancement, governed by $\gamma\dot{x}(\theta) - Rax(\theta) + Rbx^3(\theta) = Rg(\theta)$, with output SNR as the optimization index in the parameter space: $(a, b, \gamma, R) \in [0.001, 3] \times [0.01, 5] \times [0.001, 2] \times [1, 200]$. The optimal output order spectra are then converted into MTF images.
- **Duffing-MNN**: Applies the Duffing oscillator for front-end enhancement, formulated as $\ddot{x}(\theta) + R\gamma\dot{x}(\theta) - R^2ax(\theta) + R^2bx^3(\theta) = R^2g(\theta)$ with output SNR-based optimization over the same parameter space as OBSR-MNN. The resulting spectra are transformed into MTF images.
- **RGSR-MNN**: Utilizes a single robust GSR oscillator–i.e., the degenerate form of the proposed GSR array (with $m = 1$) as described in Eq. (4)–to enhance a single fault characteristic at the front end. After optimization, the order spectra are converted into MTF images.
- **RGSRA-MNN**: The proposed method employs the robust GSR array to simultaneously enhance MFCs at the front end. The resulting optimal order spectra are then used to generate MTF images.

The MTF images generated by each method are fed into an identical lightweight CNN to ensure consistent back-end feature learning and classification. Notably, unlike the proposed RGSRA-MNN, which is designed to enhance MFCs at the orders $k \times \hat{\mu}_{\text{i}}$, $k \times \hat{\mu}_{\text{o}}$, or $k \times 2\hat{\mu}_{\text{b}}$ for $k = 1, 2, 3$, the OBSR-MNN, Duffing-MNN, and RGSR-MNN methods are restricted to enhancing only a single fault component at $\hat{\mu}_{\text{i}}$, $\hat{\mu}_{\text{o}}$, $2\hat{\mu}_{\text{b}}$, respectively.

To ensure a comprehensive evaluation of all diagnostic methods, we adopt several standard performance metrics: Accuracy, ROC-AUC, Precision, Recall, and F1-score. These metrics collectively provide a multi-dimensional assessment of diagnostic accuracy, robustness, and reliability.

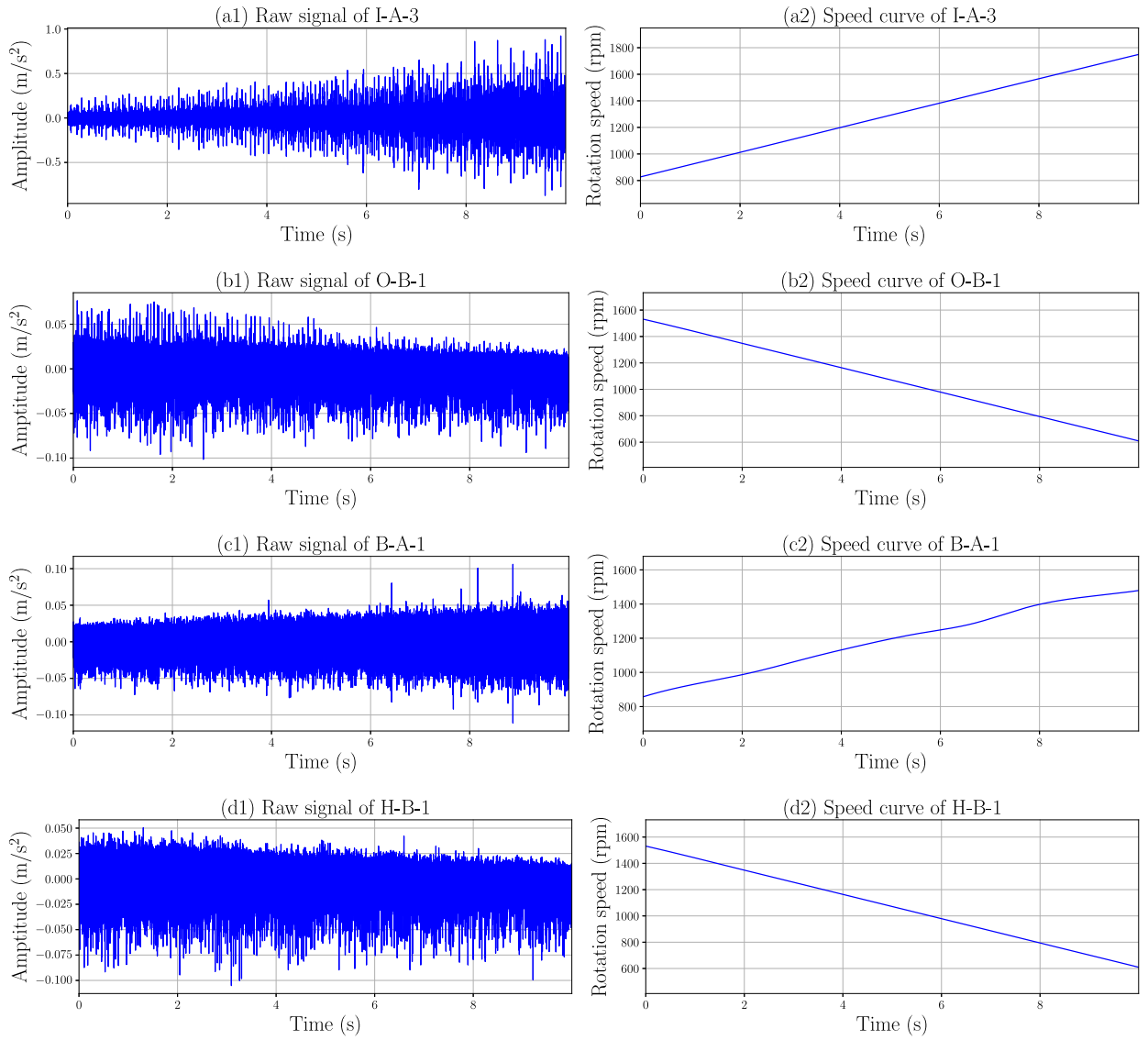

Fig. 4. The raw signals and speed curves of experimental datasets.

4.2. RGSRA-MNN architecture and module evaluation

4.2.1. Front-end MFCs enhancement

This section presents a comprehensive comparative analysis of the front-end feature enhancement capabilities of various methods, focusing on their respective optimal order spectra and MTF representations. Fig. 5 illustrates the processed signals corresponding to faulty conditions, while Fig. 6 presents the results for healthy cases. In the analysis of healthy signals, samples are divided into three hypothetical groups (1–200, 201–400, and 401–600), each artificially labeled as Inner, Outer, and Ball, respectively. For brevity, only the 1st, 201st, and 401st samples are visualized, with each representing one of the three groups.

As shown in Figs. 5(a1) and 6(a1), the COT-resampled signals exhibit minimal enhancement of fault-related features. Subsequent envelope analysis, depicted in Fig. 5(b1), reveals several distinguishable spectral peaks in the I-A-3 case; however, the O-B-1 and B-A-1 cases lack significant fault-related order components. For healthy signals, the corresponding spectra in Fig. 6(b1) display a relatively uniform energy distribution, with no salient peaks near fault characteristic orders. The MTF representations derived from these signals, shown in Figs. 5(a2)–(b4) and 6(a2)–(b4), exhibit disordered transition probability patterns with limited class discriminability.

In the case of the OBSR, illustrated in Figs. 5(c1) and 6(c1), the order spectra similarly fail to emphasize components aligned with theoretical fault orders. The corresponding MTF diagrams remain unstructured, offering limited distinguishability among fault types.

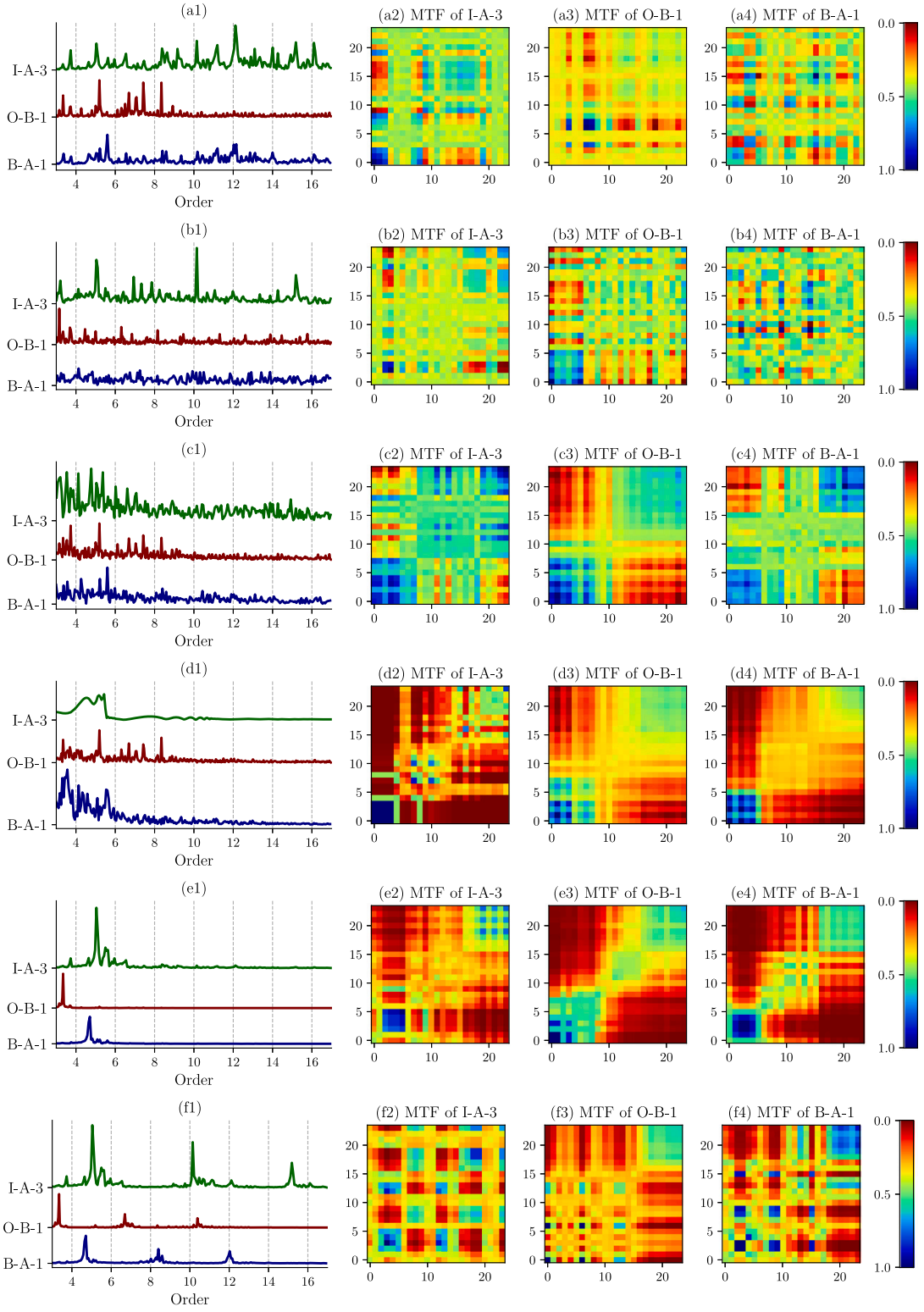

Fig. 5. The order spectra and corresponding MTF images of fault signals processed by different front-end feature enhancement methods: (a) direct COT processing, (b) angular-domain envelope analysis, (c) OBSR, (d) Duffing, (e) robust GSR, and (f) robust GSR array.

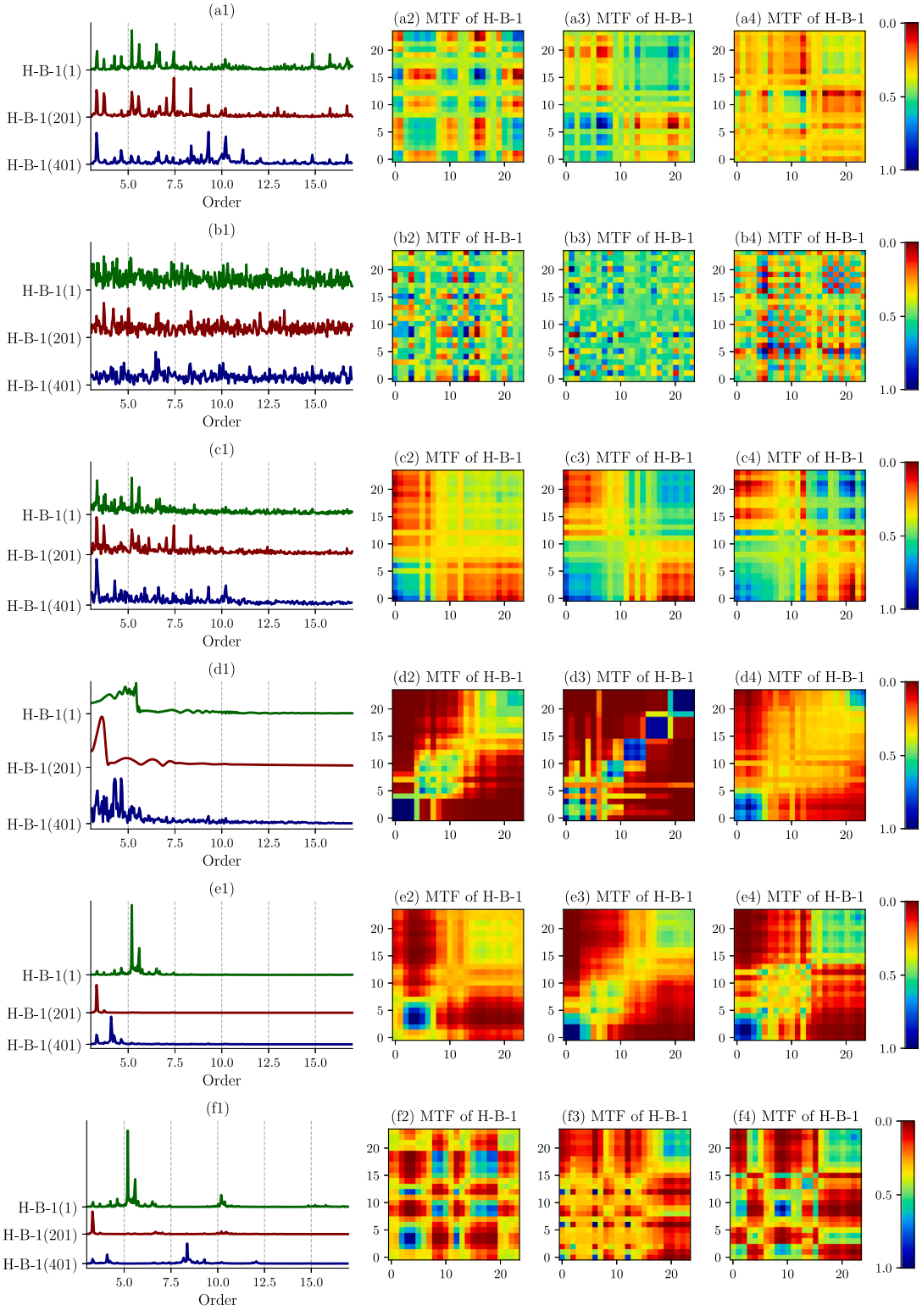

Fig. 6. The order spectra and corresponding MTF images of healthy signal processed by different front-end feature enhancement methods: (a) direct COT processing, (b) angular-domain envelope analysis, (c) OBSR, (d) Duffing, (e) robust GSR, and (f) robust GSR array.

Table 2
The optimal system parameters of different front-end feature enhancement methods.

Method	Optimal system parameters							
Dataset **I-A-3** with $\hat{\mu}_i = 5.43$								
	Order	γ	a	b	σ	λ	ω	R
OBSR	–	0.0529	0.2091	1.4081	–	–	–	41.4321
Duffing	–	0.0312	1.6014	1.1893	–	–	–	3.0670
Robust GSR	–	0.0311	–	–	0.7944	37.4547	0.4765	69.8919
Robust GSR array	$k=1$	0.0311	–	–	0.7944	37.4547	0.4765	69.8919
	$k=2$	0.0280	–	–	0.7185	59.0484	1.1718	58.3433
	$k=3$	0.0624	–	–	0.1902	87.0736	1.2446	82.3078
Dataset **O-B-1** with $\hat{\mu}_o = 3.57$								
OBSR	–	0.0153	0.1078	0.6524	–	–	–	33.9727
Duffing	–	0.6802	0.0556	1.8559	–	–	–	73.2835
Robust GSR	–	0.0105	–	–	0.1145	8.6028	0.6144	36.3615
Robust GSR array	$k=1$	0.0105	–	–	0.1145	8.6028	0.6144	36.3615
	$k=2$	0.0139	–	–	0.9544	31.1844	0.7559	60.9254
	$k=3$	0.0257	–	–	0.4115	30.3424	1.2650	52.5573
Dataset **B-A-1** with $2\hat{\mu}_b = 4.31$								
OBSR	–	0.0564	0.0433	1.0513	–	–	–	42.7549
Duffing	–	0.0108	0.0237	0.4075	–	–	–	27.1886
Robust GSR	–	0.0467	–	–	0.8410	58.1576	0.3130	82.8036
Robust GSR array	$k=1$	0.0467	–	–	0.8410	58.1576	0.3130	82.8036
	$k=2$	0.0205	–	–	0.3439	23.7630	0.7825	70.5597
	$k=3$	0.0253	–	–	0.6948	76.1707	0.9487	84.9823
Dataset **H-B-1** with hypothetical of inner race fault $\hat{\mu}_i = 5.43$								
OBSR	–	0.0389	0.0663	1.0622	–	–	–	20.7869
Duffing	–	0.0101	1.1531	0.8804	–	–	–	3.5954
Dataset **H-B-1** with hypothetical of outer race fault $\hat{\mu}_o = 3.57$								
OBSR	–	0.0628	0.0516	0.9958	–	–	–	33.5123
Duffing	–	0.1218	1.0661	0.0122	–	–	–	2.5726
Dataset **H-B-1** with hypothetical of rolling element fault $2\hat{\mu}_b = 4.31$								
OBSR	–	0.0254	0.0592	0.6734	–	–	–	41.2732
Duffing	–	0.0157	0.0399	0.8747	–	–	–	21.7952

For the Duffing (Figs. 5(d1) and 6(d1)), both faulty and healthy signals show energy concentrated primarily in low-order components, without enhancing harmonics associated with fault features. This results in significant spectral overlap across categories, which adversely affect the reliability of subsequent fault classification.

The robust GSR oscillator, as illustrated in Fig. 5(e1), effectively amplifies distinct fault features within faulty signals. However, similar order peaks also emerge in the healthy signal, as shown in Fig. 6(e1), potentially resulting in false-positive diagnoses. In comparison, the robust GSR array, shown in Fig. 5(f1), exhibits a more pronounced enhancement of multiple fault-related orders in faulty signals. Nevertheless, it also amplifies certain components in healthy signals, as evident in Fig. 6(f1). The MTF representations of both methods, presented in Figs. 5(e2)–(f4) and 6(e2)–(f4), reveal similar transitional patterns under both healthy and faulty conditions. These observations suggest that relying solely on peak-based spectral enhancement may not suffice for reliable fault detection and could lead to misinterpretation.

Table 2 summarizes the optimized parameters for each enhancement method. For both the robust GSR oscillator and robust GSR array, the optimal parameters are solely determined by the theoretical FCO $\hat{\mu}$ and remain invariant across samples operating under identical conditions, thereby requiring only a one-time optimization. Moreover, these parameters can also be directly generalized to healthy samples by assigning the corresponding hypothetical fault orders. In contrast, the OBSR and Duffing systems exhibit sample-specific parameter dependencies, necessitating individualized tuning for each input signal. For comparison, only the optimized parameters for the first sample are reported. This distinction underscores the robustness and computational efficiency of the proposed FFA index, particularly in large-scale diagnostic scenarios where extensive sample-wise tuning would be impractical.

4.2.2. Mid-end MTF configuration

In the mid-end MTF image representation, the configuration of the frequency band $[\mu_{\min}, \mu_{\max}]$ and the number of quantile bins Q critically affects both diagnostic accuracy and computational efficiency. The frequency band should encompass all potential MFCs to preserve fault-related information in the angular-domain order spectrum, while an excessively wide band increases the amplitude sequence length, raising computational cost and reducing efficiency. Similarly, quantile bins Q control the granularity of state partitioning: too few bins merge intermediate states and blur transition trajectories, whereas too many bins produce sparse transition matrices, lower the concentration of transition probability estimates, and increase the sensitivity of feature representation to minor perturbations. These considerations indicate that MTF configuration involves a trade-off between accuracy and efficiency.

Table 3
The average classification results of the RGSRA-MNN method with different mid-end MTF configurations.

Interval \ Q	2		3		5		7		10		15		Average
	Accuracy	Std	Accuracy	Std	Accuracy	Std	Accuracy	Std	Accuracy	Std	Accuracy	Std	
[4, 16]	0.9812	0.0051	0.9917	0.0043	0.9946	0.0032	0.9961	0.0075	0.9964	0.0025	0.9966	0.0033	0.9927
[3, 17]	0.9861	0.0055	0.9908	0.0048	0.9961	0.0025	0.9965	0.0035	0.9967	0.0028	0.9965	0.0031	0.9955
[2, 18]	0.9863	0.0043	0.9924	0.0045	0.9957	0.0093	0.9949	0.0127	0.9966	0.0025	0.9957	0.0056	0.9936
[1, 19]	0.9804	0.0053	0.9921	0.0050	0.9964	0.0045	0.9958	0.0038	0.9967	0.0038	0.9976	0.0025	0.9932
[0, 20]	0.9797	0.0065	0.9907	0.0039	0.9948	0.0033	0.9964	0.0031	0.9949	0.0031	0.9964	0.0037	0.9927

Table 4
The computational complexity for different lightweight models.

Model	Parameter count (M)	FLOPs (M)	Model size (MB)	Average training Per trail (s)
Tinyvit	5.07	136.17	19.57	90.80
MobileNetV4	2.50	16.86	9.63	46.10
SqueezeNet	0.74	53.76	2.86	26.40
Lightweight CNN	2.12	24.51	8.08	14.50

The results in Table 3 show that accuracy improves markedly as Q increases from 2 to 5, but further increasing Q to 15 yields only minimal gains while dramatically enlarging the transition matrix ninefold, substantially inflating computational complexity. Thus, $Q = 5$ provides an effective compromise between accuracy and efficiency. Regarding the frequency band, based on the theoretical fault characteristic orders, i.e., $k \times \hat{\mu}_{\mathrm{i}}$, $k \times \hat{\mu}_{\mathrm{o}}$, and $k \times \hat{\mu}_{\mathrm{b}}$ for $k = 1, 2, 3$, the selected band should first ensure coverage of all potential MFCs (ranging from a minimum of $1 \times \hat{\mu}_{\mathrm{o}} = 3.57$ to a maximum of $3 \times \hat{\mu}_{\mathrm{i}} = 16.29$). To accommodate possible estimation errors, a slightly wider band than the theoretical range is preferable. In the comparative analysis, fully covering bands $[3, 17]$, $[2, 18]$, $[1, 19]$, $[0, 20]$, as well as a partially covering band $[4, 16]$, are considered. The results in Table 3 show that $[1, 19]$ achieves the highest accuracy (99.64%) for $Q = 5$, but the gain over $[3, 17]$ (99.61%) is marginal. Moreover, Table 3 indicates that $[3, 17]$ provides the highest average accuracy (99.55%) across different Q values. Based on this comprehensive analysis, which balances diagnostic accuracy and efficiency, we adopt the MTF configuration of frequency band $[3, 17]$ and quantile bins $Q = 5$ for all subsequent fault diagnosis experiments.

4.2.3. Back-end lightweight CNN

In this subsection, we evaluate the overall advantages of back-end lightweight CNN by comparing the computational complexity and classification performance with representative lightweight models: TinyViT, MobileNetV4, and SqueezeNet. The computational complexity is assessed using four fundamental metrics: (i) parameter count, (ii) floating point operations (FLOPs), (iii) model size, and (iv) average training time per trail. Classification performance is evaluated under three noise scenarios: original datasets (I-A-3, O-B-1, B-A-1, and H-B-1), and the datasets contaminated with WGNs corresponding to input SNR degradations of 6.17 dB and 9.17 dB, respectively.

Table 4 summarizes the computational complexity of the lightweight models. SqueezeNet achieves the most compact representation, with only 0.74 million (M) parameters, 53.76 M FLOPs, and a 2.86 megabyte (MB) model size. TinyViT exhibits the highest complexity, with 5.07 M parameters, 136.17 M FLOPs, and a 19.57 MB model size, reflecting the computational overhead of transformer-based architectures. MobileNetV4 presents a balanced profile, with 2.50 M parameters, 16.86 M FLOPs, and a 9.63 MB model size. The lightweight CNN in the proposed RGSRA-MNN framework achieves a well-balanced complexity, with 2.12 M parameters, 24.51 M FLOPs, and an 8.08 MB model size, maintaining moderate computational demands. It also demonstrates the most efficient training, completing one trial in 14.50 s, compared with 90.80 s for TinyViT, 46.10 s for MobileNetV4, and 26.40 s for SqueezeNet. To ensure comparability, all models are evaluated using the identical front-end MFC enhancement and mid-end MTF transformation employed in the RGSRA-MNN framework. The results under different noise levels are presented in Table 5. On the original datasets, the lightweight CNN achieves the highest classification accuracy of 99.69%, followed by MobileNetV4 (99.43%), TinyViT (99.40%), and SqueezeNet (99.23%). As noise intensity increases, all models experience some degradation in accuracy; however, the proposed method consistently maintains superior performance. Even under severe input SNR degradation of 9.17 dB, the lightweight CNN sustains an accuracy of 95.53%. Striking an effective balance between accuracy and efficiency, the lightweight CNN demonstrates strong potential for practical industrial deployment, particularly when combined with the front-end robust GSR array and MTF image representation, which underpins its distinctive advantage.

4.3. Diagnostic results

This section evaluates the classification performance under three distinct noise conditions. First, a lightweight CNN is employed to classify features extracted from the original, noise-free signals. To further investigate robustness against noise interference, WGN is added to the original signals at two different noise intensities: $D = 0.005$ and $D = 0.01$, corresponding to input SNR degradations of 6.17 dB and 9.17 dB, respectively. Classification is then performed on the noise-contaminated signals to assess the degradation in performance and the resilience of the proposed method under adverse cases.

For the first case, the t-SNE visualizations in Fig. 7 illustrate the classification performance of various methods under noise-free conditions. In Fig. 7(b)–(d), the EMNN, OBSR-MNN, and Duffing-MNN methods exhibit substantial class overlap, making it difficult to distinguish between different fault types. The RGSR-MNN, shown in Fig. 7(e), achieves better separation and correctly classifies

Table 5
The average classification results for different lightweight models.

Lightweight model	Accuracy		ROC-AUC		Precision		Recall		F1-score		Input SNR
	Average	Std	Average	Std	Average	Std	Average	Std	Average	Std	degradation (dB)
Tinyvit	0.9940	0.0019	0.9998	0.0002	0.9941	0.0019	0.9940	0.0019	0.9940	0.0019	–
	0.9468	0.0063	0.9935	0.0021	0.9474	0.0062	0.9468	0.0063	0.9463	0.0067	6.17
	0.9347	0.0055	0.9902	0.0024	0.9360	0.0052	0.9347	0.0055	0.9343	0.0058	9.17
MobileNetV4	0.9943	0.0140	0.9998	0.0009	0.9949	0.0117	0.9943	0.0140	0.9943	0.0139	–
	0.9649	0.0128	0.9974	0.0026	0.9658	0.0110	0.9649	0.0128	0.9647	0.0129	6.17
	0.9547	0.0030	0.9940	0.0009	0.9548	0.0029	0.9547	0.0030	0.9544	0.0031	9.17
SqueezeNet	0.9923	0.0133	0.9998	0.0005	0.9928	0.0117	0.9923	0.0133	0.9922	0.0136	–
	0.9483	0.0314	0.9951	0.0033	0.9528	0.0208	0.9483	0.0314	0.9485	0.0303	6.17
	0.9110	0.0610	0.9883	0.0095	0.9219	0.0387	0.9110	0.0610	0.9085	0.0642	9.17
Lightweight CNN	0.9969	0.0026	1.0000	0.0000	0.9970	0.0025	0.9969	0.0026	0.9969	0.0026	–
	0.9696	0.0078	0.9981	0.0009	0.9698	0.0076	0.9696	0.0078	0.9695	0.0078	6.17
	0.9553	0.0082	0.9955	0.0012	0.9560	0.0077	0.9553	0.0082	0.9553	0.0081	9.17

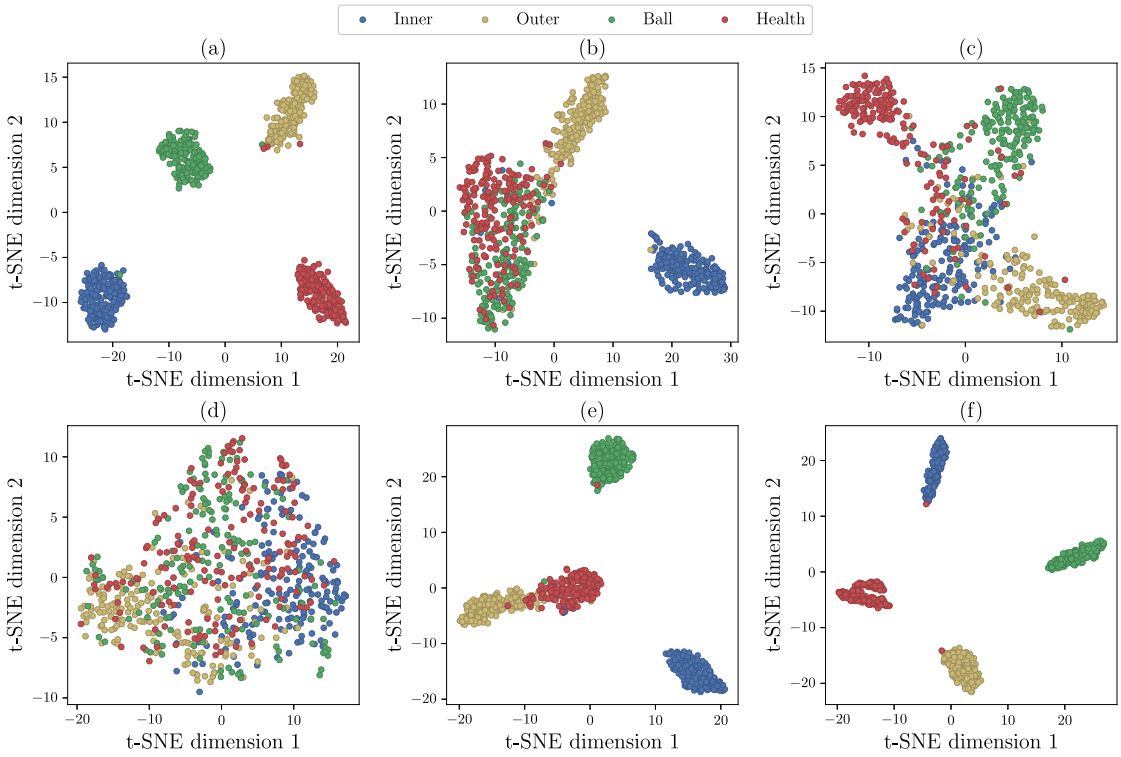

Fig. 7. The t-SNE clustering results of different methods under original signal condition: (a) MNN, (b) EMNN, (c) OBSR-MNN, (d) Duffing-MNN, (e) RGSR-MNN, and (f) RGSRA-MNN.

most fault signals; however, it still shows noticeable confusion between healthy and faulty states. The baseline MNN method, presented in Fig. 7(a), also suffers from some misclassification. In contrast, the proposed RGSRA-MNN, in Fig. 7(f), demonstrates superior class separability, with only two samples misaligned near other fault categories. Fig. 8 displays the ROC curves and corresponding performance metrics for all methods, further corroborating the classification results.

To ensure statistical reliability, each method is trained over 20 independent trials, with the average confusion matrices shown in Fig. 9. Under the original signal condition, both MNN and RGSRA-MNN, shown in Fig. 9(a) and (f), respectively, achieve high classification accuracy, with each fault category exceeding 99%. Among these, RGSRA-MNN exhibits the most consistent and superior overall performance. The RGSR-MNN method, in Fig. 9(e), performs less effectively than both MNN and RGSRA-MNN. Notably, the EMNN method, in Fig. 9(b), achieves acceptable accuracy for inner and outer race faults but struggles to correctly classify rolling element faults and healthy samples, with accuracy rates of only 66.58% and 64.39%, respectively. The OBSR-MNN and Duffing-MNN, shown in Fig. 9(c) and (d), perform poorly, with classification performance close to random guessing.

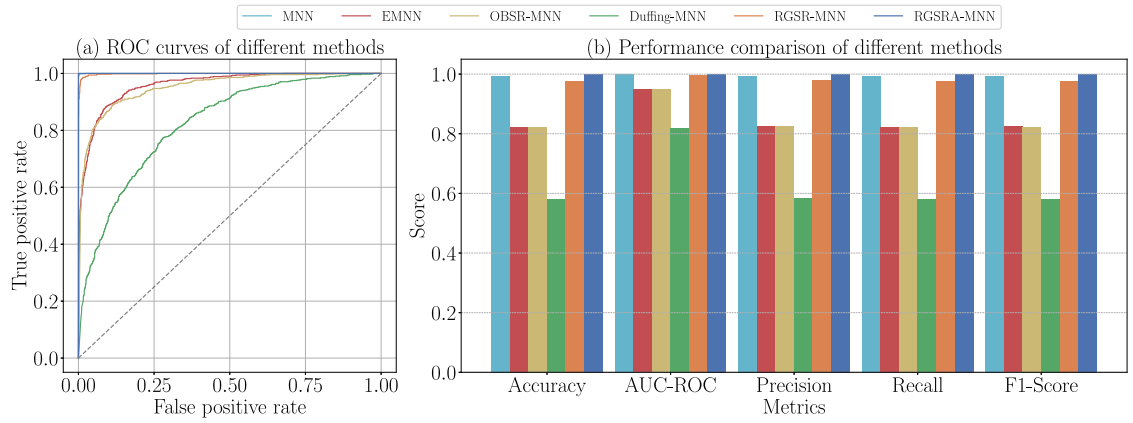

Fig. 8. The comparison of diagnostic performance for different methods under original signal condition.

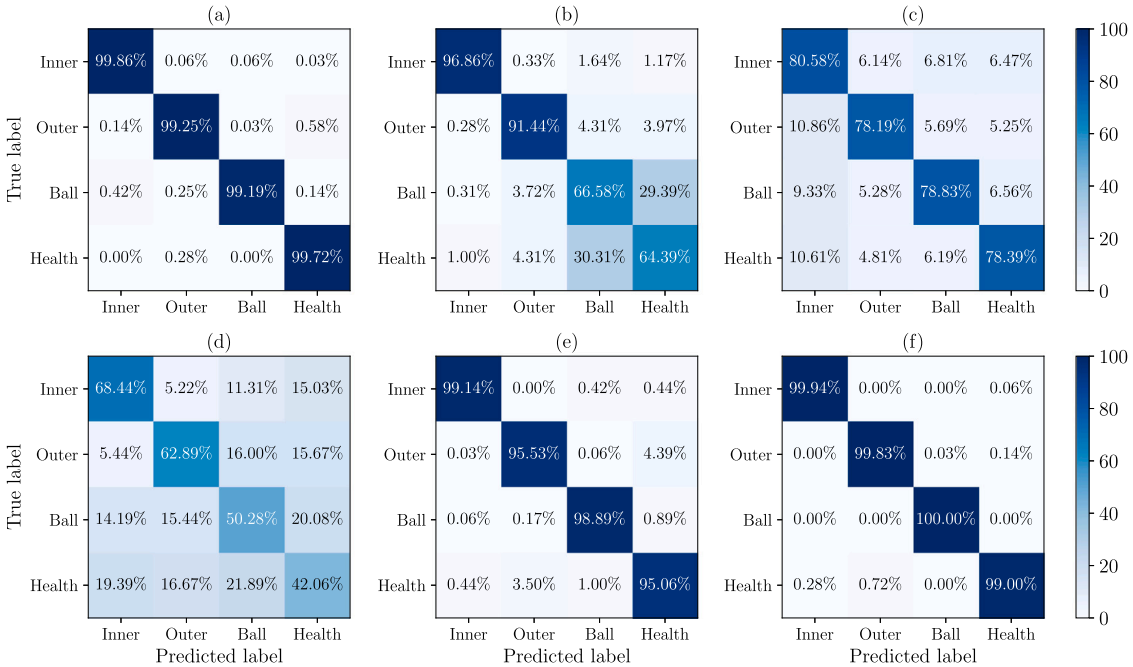

Fig. 9. The average confusion matrices of different methods under original signal condition: (a) MNN, (b) EMNN, (c) OBSR-MNN, (d) Duffing-MNN, (e) RGSR-MNN, and (f) RGSRA-MNN.

Table 6
The average classification results of different methods under original signal condition.

Method	Accuracy		ROC-AUC		Precision		Recall		F1-score	
	Average	Std	Average	Std	Average	Std	Average	Std	Average	Std
MNN	0.9951	0.0099	0.9999	0.0005	0.9952	0.0094	0.9951	0.0099	0.9951	0.0099
EMNN	0.7982	0.0139	0.9394	0.0062	0.8007	0.0144	0.7982	0.0139	0.7985	0.0139
OBSR-MNN	0.7900	0.0147	0.9431	0.0058	0.7943	0.0159	0.7900	0.0147	0.7904	0.0149
Duffing-MNN	0.5592	0.0150	0.8006	0.0105	0.5572	0.0156	0.5592	0.0150	0.5565	0.0156
RGSR-MNN	0.9715	0.0047	0.9982	0.0006	0.9720	0.0044	0.9715	0.0047	0.9715	0.0046
RGSRA-MNN	**0.9969**	0.0026	**1.0000**	0.0000	**0.9970**	0.0025	**0.9969**	0.0026	**0.9969**	0.0026

The averaged evaluation metrics on the test sets are reported in Table 6. Consistent with the visualization and confusion matrix results, the proposed RGSRA-MNN achieves the highest scores across all evaluation criteria, with minimal variance across trials, indicating both high accuracy and robust stability.

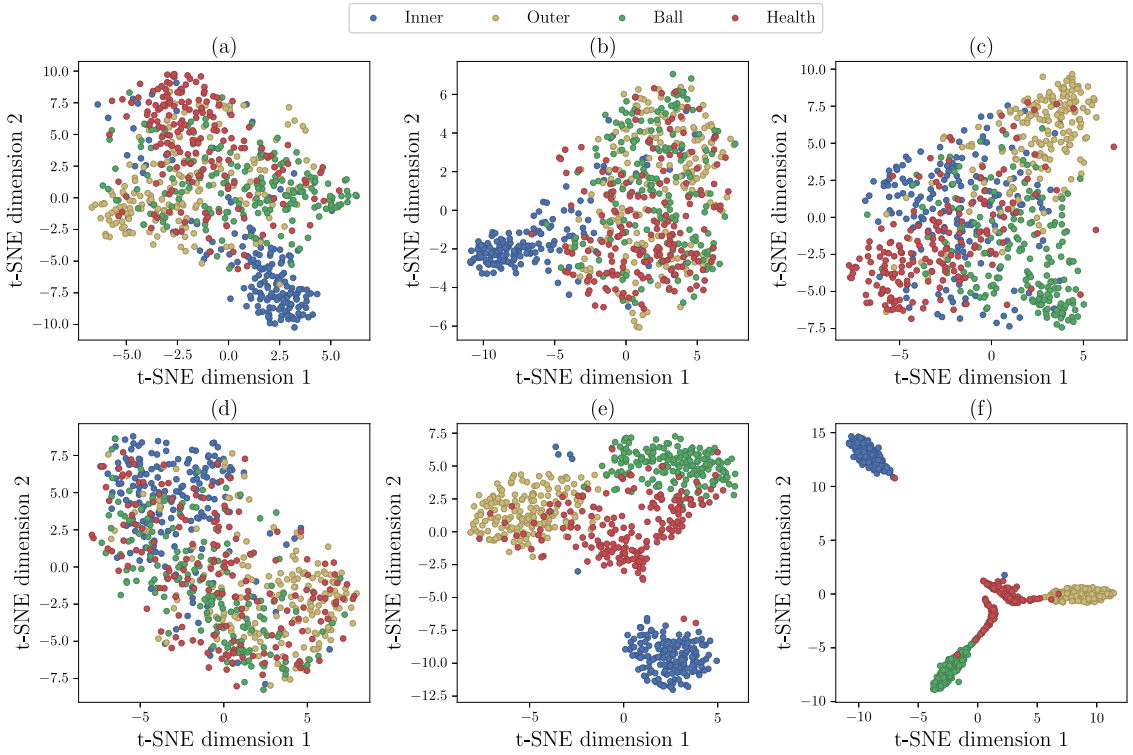

Fig. 10. The t-SNE clustering results of different methods under 6.17 dB input SNR degradation (by adding WGN with an intensity of $D = 0.005$): (a) MNN, (b) EMNN, (c) OBSR-MNN, (d) Duffing-MNN, (e) RGSR-MNN, and (f) RGSRA-MNN.

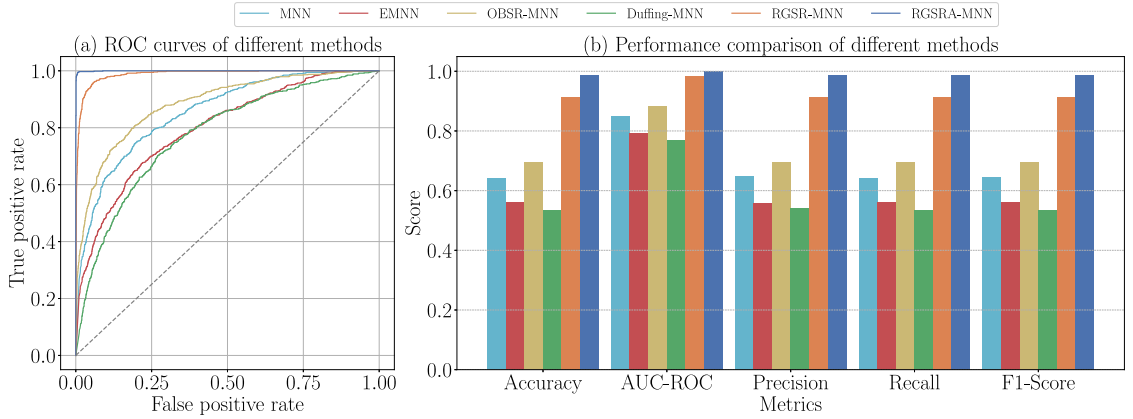

Fig. 11. The comparison of diagnostic performance for different methods under 6.17 dB input SNR degradation (by adding WGN with an intensity of $D = 0.005$).

Under the challenging scenario of a 6.17 dB input SNR degradation, the t-SNE visualizations in Fig. 10 depict the feature distributions. As illustrated in Fig. 10(a)–(d), the MNN, EMNN, OBSR-MNN, and Duffing-MNN fail to produce well-separated clusters, particularly between healthy and faulty categories. Although the RGSR-MNN shown in Fig. 10(e) achieves improved separation, considerable overlap remains. In contrast, the proposed RGSRA-MNN, in Fig. 10(f), yields the most distinct and compact clustering, indicating superior feature extraction capability under noisy conditions.

Accordingly, the ROC curves and performance metrics are presented in Fig. 11, while the average confusion matrices across 20 trials are shown in Fig. 12. As seen in Fig. 12(e), RGSR-MNN achieves classification accuracies above 90% for inner race and rolling element faults but performs less satisfactorily for outer race (88.06%) and healthy samples (74.06%). By contrast, the proposed RGSRA-MNN, in Fig. 12(f), maintains consistently high classification performance across all categories: 98.94% (inner race), 97.31% (outer race), 98.92% (rolling element), and 92.67% (healthy). The corresponding averaged performance metrics are reported in Table



Fig. 12. The average confusion matrices of different methods under 6.17 dB input SNR degradation (by adding WGN with an intensity of $D = 0.005$): (a) MNN, (b) EMNN, (c) OBSR-MNN, (d) Duffing-MNN, (e) RGSR-MNN, and (f) RGSRA-MNN.

Table 7
The average classification results of different methods under 6.17 dB input SNR degradation (by adding WGN with an intensity of $D=0.005$).

Method	Accuracy		ROC-AUC		Precision		Recall		F1-score	
	Average	Std	Average	Std	Average	Std	Average	Std	Average	Std
MNN	0.5817	0.0786	0.8094	0.0721	0.5759	0.1202	0.5817	0.0786	0.5735	0.1107
EMNN	0.5230	0.0163	0.7669	0.0123	0.5239	0.0188	0.5230	0.0163	0.5215	0.0173
OBSR-MNN	0.5966	0.1468	0.8694	0.1382	0.5716	0.2146	0.5966	0.1468	0.5729	0.1997
Dufffing-MNN	0.5100	0.0148	0.7572	0.0119	0.5083	0.0132	0.5100	0.0148	0.5065	0.0130
RGSR-MNN	0.8842	0.0147	0.9783	0.0040	0.8858	0.0151	0.8842	0.0147	0.8828	0.0149
RGSRA-MNN	**0.9696**	0.0078	**0.9981**	0.0009	**0.9698**	0.0076	**0.9696**	0.0078	**0.9695**	0.0078

Table 8
The average classification results of different methods under 9.17 dB input SNR degradation (by adding WGN with an intensity of $D=0.01$).

Method	Accuracy		ROC-AUC		Precision		Recall		F1-score	
	Average	Std	Average	Std	Average	Std	Average	Std	Average	Std
MNN	0.4489	0.0855	0.6955	0.0835	0.4228	0.1525	0.4489	0.0855	0.4257	0.1381
EMNN	0.4873	0.0173	0.7349	0.0110	0.4871	0.0193	0.4873	0.0173	0.4847	0.0180
OBSR-MNN	0.5513	0.0717	0.7822	0.0660	0.5432	0.1123	0.5513	0.0717	0.5419	0.1033
Duffing-MNN	0.4865	0.0570	0.7367	0.0553	0.4743	0.0959	0.4865	0.0570	0.4761	0.0879
RGSR-MNN	0.8837	0.0164	0.9787	0.0047	0.8852	0.0141	0.8837	0.0164	0.8836	0.0155
RGSRA-MNN	**0.9553**	0.0082	**0.9955**	0.0012	**0.9560**	0.0077	**0.9553**	0.0082	**0.9553**	0.0081

7, where RGSRA-MNN achieves a robust overall accuracy of 96.96%. In comparison, the performance of other methods deteriorates substantially: MNN drops to 58.17%, EMNN to 52.30%, OBSR-MNN to 59.66%, Duffing-MNN to 51.00%, and RGSR-MNN to 88.42%.

Under more severe input SNR degradation 9.17 dB, the separability of fault categories becomes even less pronounced for most methods, as shown in the t-SNE visualizations in Fig. 13. The corresponding ROC curves and performance metrics are presented in Fig. 14. The average confusion matrices in Fig. 15 reveal widespread misclassifications across the baseline and conventional enhancement methods. Nevertheless, the proposed RGSRA-MNN maintains high classification accuracy across all fault types, achieving 97.64% (inner race), 95.86% (outer race), 97.81% (rolling element), and 90.83% (healthy). As reported in Table 8, RGSRA-MNN sustains an overall accuracy above 95%, demonstrating remarkable noise robustness. In contrast, the performance of MNN, EMNN, OBSR-MNN, and Duffing-MNN further deteriorates to 44.89%, 48.73%, 55.13%, and 48.65%, respectively, while RGSR-MNN decreases to 88.37%. These results consistently demonstrate the superior diagnostic reliability and noise resilience of the proposed RGSR-MNN under certain challenging conditions. The optimal system parameters for the different methods across

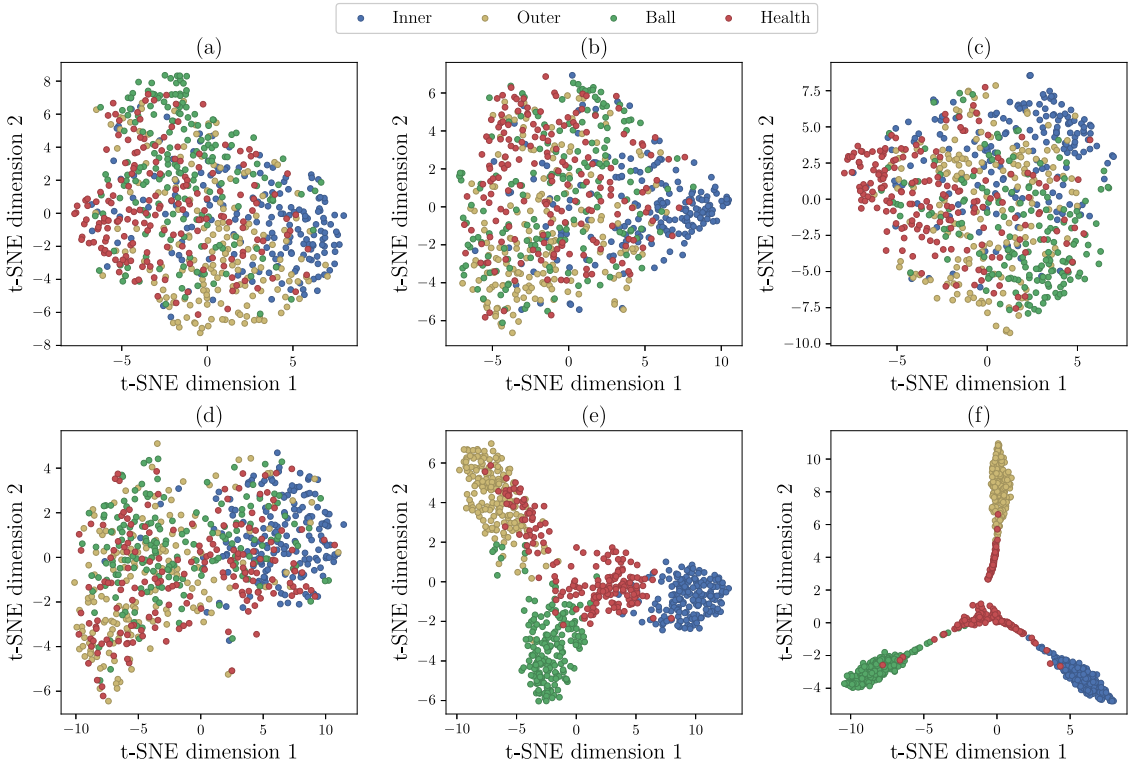

Fig. 13. The t-SNE clustering results of different methods under 9.17 dB input SNR degradation (by adding WGN with an intensity of $D = 0.01$): (a) MNN, (b) EMNN, (c) OBSR-MNN, (d) Duffing-MNN, (e) RGSR-MNN, and (f) RGSRA-MNN.

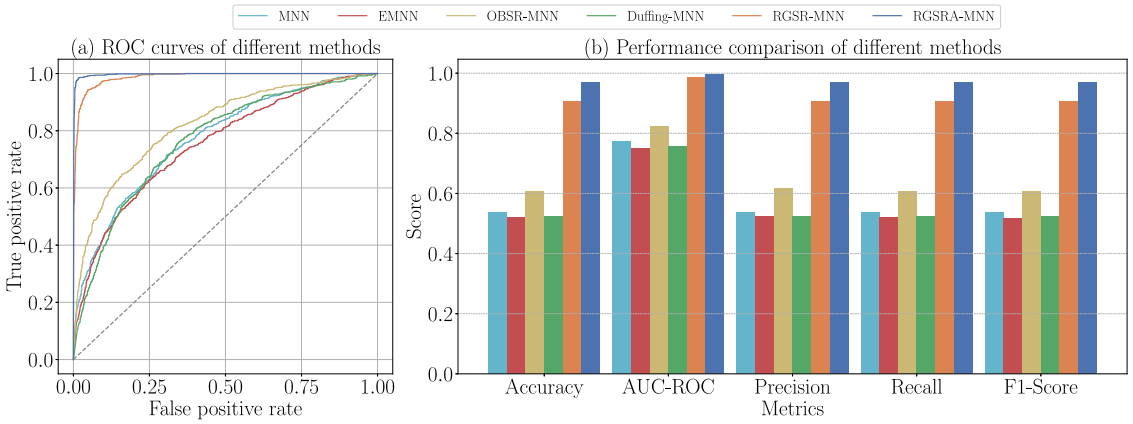

Fig. 14. The comparison of diagnostic performance for different methods under 9.17 dB input SNR degradation (by adding WGN with an intensity of $D = 0.01$).

various cases are listed in Tables 2, 9, and 10. The corresponding optimization details are provided in the explanation of Table 2 in Section 4.2.1.

Following the classification performance analysis, we further provide a comprehensive comparison of computational efficiency across different diagnostic methods. Specifically, we record the processing time during both training and testing phases, including (i) front-end feature enhancement, (ii) mid-end MTF transformation, (iii) back-end intelligent classification, as well as the total execution time on 1680 training samples and the average inference time per testing sample. The detailed results are summarized in Table 11. The OBSR-MNN and Duffing-MNN methods exhibit very low computational efficiency during both training and testing, mainly due to the significant time overhead caused by front-end system optimization. In contrast, RGSR-MNN achieves the highest time efficiency (excluding MNN and EMNN, which bypass front-end feature enhancement altogether). Although the proposed RGSRA-MNN does not deliver the shortest overall execution time, it maintains efficiency comparable to the three fastest methods



Fig. 15. The average confusion matrices of different methods under 9.17 dB input SNR degradation (by adding WGN with an intensity of $D = 0.01$): (a) MNN, (b) EMNN, (c) OBSR-MNN, (d) Duffing-MNN, (e) RGSR-MNN, and (f) RGSRA-MNN.

while offering distinct advantages in diagnostic accuracy and noise robustness. Importantly, its average inference time per test sample remains sufficiently low for practical deployment, thereby avoiding latency bottlenecks and achieving a favorable balance between computational efficiency and diagnostic reliability.

4.4. Extended performance validation

4.4.1. Parameter transferability across datasets

The preceding analysis shows that, in the front-end MFCs enhancement process, the optimization of the robust GSR array is guided by the theoretical FFA index, which relies solely on the prior information $\hat{\mu}$. This prior remains constant under fixed equipment parameters and is independent of real-time operating conditions. When combined with the back-end lightweight CNN, the proposed RGSRA-MNN diagnostic framework is thus expected to exhibit favorable transferability across different scenarios. In this subsection, we evaluate the cross-dataset transferability of the proposed method under conditions with identical theoretical fault orders.

For this purpose, validation datasets with different speed profiles — but identical theoretical fault orders — are also selected from [67]. Specifically, they include: (i) I-B-1: inner race fault during deceleration, (ii) O-A-1: outer race fault during acceleration, (iii) B-B-1: rolling element fault during deceleration, and (iv) H-A-1: healthy signal during acceleration. All datasets are sampled at 20 kHz over 10 s intervals, consistent with the original datasets I-A-3, O-B-1, B-A-1, and H-B-1. Preprocessing and segmentation procedures are kept identical to those used for the original datasets, and the optimized parameters obtained from the original datasets are directly transferred without re-optimization. The average performance across 20 trials is reported in Table 12. The transferred parameters achieve an average accuracy of 99.73%, which is nearly identical to the 99.69% obtained on the original datasets.

Furthermore, we assess parameter transferability under noisy conditions by adding WGN with intensities $D = 0.005$ and 0.01 to the validation datasets (I-B-1, O-A-1, B-B-1, and H-A-1), corresponding to input SNR degradation of 6.17 dB and 9.17 dB, respectively. The transferred parameters continue to deliver robust diagnostic performance, achieving accuracies of 94.99% and 93.85%. Compared to the accuracies on the original datasets, the performance degradation remains within 2% across all tested conditions. These results demonstrate the stability and reliability of parameter transferability, while also highlighting its potential for broader cross-dataset applications.

4.4.2. Robustness under diverse noise conditions

In this subsection, we extend the robustness evaluation beyond WGN to more comprehensively assess the proposed method under diverse noise environments. Specifically, we consider two representative types of industrial noise: pink noise and impulsive noise, which more accurately reflect practical interference patterns in mechanical systems. Pink noise, characterized by a $1/f$ power spectral density, is widely used to simulate low-frequency industrial disturbances. Impulsive noise, on the other hand, is defined by abrupt high-amplitude transients and is typically employed to emulate impact events and machinery shocks.

Table 9
The optimal system parameters of different front-end feature enhancement methods under 6.17 dB input SNR degradation (by adding WGN with an intensity of $D=0.005$).

Method	Optimal system parameters							
Dataset **I-A-3** with $\hat{\mu}_i=5.43$								
	Order	γ	a	b	σ	λ	ω	R
OBSR	–	0.0235	0.1590	1.1279	–	–	–	51.3909
Duffing	–	0.0399	0.0385	1.5576	–	–	–	36.5133
Robust GSR	–	0.0173	–	–	0.3153	39.7422	0.3192	103.9633
Robust GSR array	$k=1$	0.0173	–	–	0.3153	39.7422	0.3192	103.9633
	$k=2$	0.0109	–	–	0.4629	8.2335	0.4496	148.6945
	$k=3$	0.0115	–	–	0.6341	8.5093	1.2429	85.3875
Dataset **O-B-1** with $\hat{\mu}_o=3.57$								
OBSR	–	0.0207	0.5357	1.3857	–	–	–	54.6761
Duffing	–	0.6602	0.0657	1.5875	–	–	–	38.0771
Robust GSR	–	0.0015	–	–	0.1492	66.7793	0.5052	44.9764
Robust GSR array	$k=1$	0.0015	–	–	0.1492	66.7793	0.5052	44.9764
	$k=2$	0.0106	–	–	0.4182	12.7033	0.6438	68.0842
	$k=3$	0.0016	–	–	0.4767	32.3753	0.7183	93.1163
Dataset **B-A-1** with $2\hat{\mu}_b=4.31$								
OBSR	–	0.0409	0.3166	1.0116	–	–	–	75.2020
Duffing	–	0.0199	0.0185	0.6756	–	–	–	21.2015
Robust GSR	–	0.0102	–	–	0.1685	34.8543	0.4872	57.6085
Robust GSR array	$k=1$	0.0102	–	–	0.1685	34.8543	0.4872	57.6085
	$k=2$	0.0205	–	–	0.0252	29.2566	0.7014	83.1440
	$k=3$	0.0131	–	–	0.4645	57.7447	1.0850	74.0671
Dataset **H-B-1** with hypothetical of inner race fault $\hat{\mu}_i=5.43$								
OBSR	–	0.0528	0.1726	0.5674	–	–	–	48.7438
Duffing	–	0.0736	0.0148	0.4415	–	–	–	36.6391
Dataset **H-B-1** with hypothetical of outer race fault $\hat{\mu}_o=3.57$								
OBSR	–	0.0548	0.3102	0.8409	–	–	–	96.9775
Duffing	–	0.3019	0.0396	1.2945	–	–	–	14.9951
Dataset **H-B-1** with hypothetical of rolling element fault $2\hat{\mu}_b=4.31$								
OBSR	–	0.0235	0.7506	1.8747	–	–	–	92.8836
Duffing	–	0.0849	0.0136	0.0849	–	–	–	20.6921

The proposed RGSRA-MNN method is evaluated under these two noise scenarios across all diagnostic metrics. In the first scenario, the addition of pink noise leads to input SNR degradations of 6.41 dB (Case 1) and 9.05 dB (Case 2). In the second scenario, the inclusion of impulsive noise results in SNR degradations of 6.17 dB (Case 3) and 9.51 dB (Case 4). The average performance across 20 trials under these conditions is summarized in Table 13. Under pink noise conditions, the proposed method achieves an accuracy of 98.27% at an SNR degradation of 6.41 dB, which even exceeds its performance (96.96%) under the WGN scenario with a similar degradation. Under the more severe pink noise condition (9.05 dB input SNR degradation), the accuracy remains above 90%, demonstrating clear superiority over other methods evaluated under comparable WGN conditions (see Table 7 with 6.17 dB SNR degradation). Similarly, robust performance is also maintained under impulsive noise conditions, yielding accuracies of 94.77% and 90.23% for 6.17 dB and 9.51 dB degradations, respectively. These results confirm the resilience of the proposed method across diverse noise types, highlighting both its robustness and its potential for practical deployment in complex industrial environments.

4.4.3. Adaptability under multi-fault scenarios

In practical industrial applications, concurrent compound fault conditions are frequently encountered, particularly when equipment is subjected to prolonged operation or harsh environments, where multiple bearing components may deteriorate simultaneously [68]. To evaluate the applicability of the proposed method under such conditions, we extend the diagnostic analysis by incorporating the compound fault signal C-A-1 from [67], recorded under acceleration conditions. This dataset is combined with the previously considered single-fault datasets (I-A-3, O-B-1, B-A-1) and the healthy dataset (H-B-1), forming a five-class diagnostic task. The compound fault signal exhibits simultaneous fault characteristics of the inner race, outer race, and rolling elements. To address this multi-fault scenario, the robust GSR array in the front-end is tailored to enhance MFCs, namely $\hat{\mu}_i$, $\hat{\mu}_o$, and $2\hat{\mu}_b$, together with their second- and third-order harmonics. This design enables the joint representation of overlapping fault signatures and supports accurate classification in compound fault environments.

The diagnostic results are illustrated in Fig. 16, where Fig. 16(a) shows the t-SNE visualization from a single trial and Fig. 16(b) presents the confusion matrix averaged over 20 trials. The results indicate consistently high diagnostic performance across all fault categories, with class accuracies generally exceeding 99% and the outer race fault class even reaching perfect recognition. These findings confirm the robustness and adaptability of the proposed RGSRA-MNN method in effectively handling compound fault conditions commonly encountered in long-term industrial operations or harsh environments.

Table 10
The optimal system parameters of different front-end feature enhancement methods under 9.17 dB input SNR degradation (by adding WGN with an intensity of $D=0.01$).

Method	Optimal system parameters							
Dataset **I-A-3** with $\hat{\mu}_i=5.43$								
	Order	γ	a	b	σ	λ	ω	R
OBSR	–	0.0486	0.4608	1.4481	–	–	–	58.5151
Duffing	–	0.0164	0.4645	0.9195	–	–	–	5.8008
Robust GSR	–	0.0100	–	–	0.0948	32.7402	0.5768	58.0253
Robust GSR array	$k=1$	0.0100	–	–	0.0948	32.7402	0.5768	58.0253
	$k=2$	0.0100	–	–	0.3241	11.0738	0.7825	85.7089
	$k=3$	0.0102	–	–	0.1375	21.3795	1.3018	76.8928
Dataset **O-B-1** with $\hat{\mu}_o=3.57$								
OBSR	–	0.0338	0.7807	1.6658	–	–	–	88.8975
Duffing	–	0.0103	0.0201	0.5856	–	–	–	9.8420
Robust GSR	–	0.0100	–	–	0.2561	10.7731	0.4765	46.4716
Robust GSR array	$k=1$	0.0100	–	–	0.2561	10.7731	0.4765	46.4716
	$k=2$	0.0102	–	–	0.6997	56.7798	0.6752	66.8157
	$k=3$	0.0110	–	–	0.2583	27.5463	1.0842	62.0455
Dataset **B-A-1** with $2\hat{\mu}_b=4.31$								
OBSR	–	0.0160	0.8040	1.4239	–	–	–	61.2513
Duffing	–	0.0117	0.0212	0.0934	–	–	–	18.1503
Robust GSR	–	0.0100	–	–	0.0786	36.8990	0.3782	74.4951
Robust GSR array	$k=1$	0.0100	–	–	0.0786	36.8990	0.3782	74.4951
	$k=2$	0.0100	–	–	0.3479	7.0417	0.6454	82.9967
	$k=3$	0.0100	–	–	0.5997	51.8667	1.0847	75.1009
Dataset **H-B-1** with hypothetical of inner race fault $\hat{\mu}_i=5.43$								
OBSR	–	0.0394	1.0230	1.7734	–	–	–	132.1085
Duffing	–	0.0136	0.0206	0.0838	–	–	–	21.7090
Dataset **H-B-1** with hypothetical of outer race fault $\hat{\mu}_o=3.57$								
OBSR	–	0.0355	0.7364	1.0833	–	–	–	118.4797
Duffing	–	0.0115	0.0205	0.0205	–	–	–	23.7225
Dataset **H-B-1** with hypothetical of rolling element fault $2\hat{\mu}_b=4.31$								
OBSR	–	0.0295	0.4029	0.7683	–	–	–	59.8852
Duffing	–	0.0118	0.0219	1.2429	–	–	–	10.9729

Table 11
The comparison of computational efficiency for different methods.

	Method	Front-end (s)	Mid-end (s)	Back-end (s)	Total (s)
Training (1680 samples)	MNN	–	26.0534	14.4250	40.4784
	EMNN	–	26.3410	14.4657	40.8067
	OBSR-MNN	6.0836×10^4	26.0429	14.6444	6.0877×10^4
	Duffing-MNN	7.5901×10^4	26.4049	14.4968	7.5942×10^4
	RGSR-MNN	16.2960	26.0707	14.4486	56.8153
	RGSRA-MNN	50.9600	26.1289	14.6110	91.6999
Testing (per sample)	MNN	–	0.0125	0.0031	0.0156
	EMNN	–	0.0110	0.0030	0.0140
	OBSR-MNN	33.5955	0.0121	0.0030	33.6106
	Duffing-MNN	46.0957	0.0114	0.0035	46.1106
	RGSR-MNN	0.0097	0.0130	0.0034	0.0261
	RGSRA-MNN	0.0303	0.0111	0.0030	0.0444

5. Conclusion

In this study, we proposed a fast intelligent fault diagnosis framework that integrates a robust GSR array, MTF representation, and a lightweight CNN to enable accurate fault classification under variable-speed conditions. The proposed method achieves an effective balance between diagnostic accuracy and computational efficiency, offering a practical and scalable solution for large-scale industrial condition monitoring. Extensive experimental evaluations validate the superiority of the proposed framework. It consistently outperformed all baseline models under both original and noise-contaminated conditions. Notably, under a 9.17 dB input SNR degradation caused by WGN, the accuracy of the baseline MNN method declined sharply by 54.62% (from 99.51% to 44.89%), whereas our method maintained a high accuracy of 95.53%. Similarly, the performance of the RGSR-MNN method — based on a single GSR oscillator — declined from 97.15% to 88.37%. Moreover, the extended validation confirms the robustness of

Table 12
The average classification results of the RGSRA-MNN method with parameter transferability across datasets under varying WGN levels.

	Accuracy		ROC-AUC		Precision		Recall		F1-score		Input SNR
	Average	Std	Average	Std	Average	Std	Average	Std	Average	Std	degradation (dB)
Original datasets	0.9969	0.0026	1.0000	0.0000	0.9970	0.0025	0.9969	0.0026	0.9969	0.0026	–
	0.9696	0.0078	0.9981	0.0009	0.9698	0.0076	0.9696	0.0078	0.9695	0.0078	6.17
	0.9553	0.0082	0.9955	0.0012	0.9560	0.0077	0.9553	0.0082	0.9553	0.0081	9.17
Transferred datasets	0.9973	0.0036	1.0000	0.0000	0.9974	0.0034	0.9973	0.0036	0.9973	0.0036	–
	0.9499	0.0090	0.9948	0.0013	0.9504	0.0086	0.9499	0.0090	0.9496	0.0091	6.17
	0.9385	0.0108	0.9936	0.0019	0.9391	0.0102	0.9385	0.0108	0.9382	0.0108	9.17

Table 13
The average classification results of the RGSRA-MNN method under diverse noise conditions.

Scenarios	Accuracy		ROC-AUC		Precision		Recall		F1-score		Input SNR
	Average	Std	Average	Std	Average	Std	Average	Std	Average	Std	degradation (dB)
Case 1	0.9827	0.0064	0.9993	0.0007	0.9828	0.0063	0.9827	0.0064	0.9827	0.0065	6.41
Case 2	0.9026	0.0094	0.9816	0.0029	0.9027	0.0093	0.9026	0.0094	0.9015	0.0098	9.05
Case 3	0.9477	0.0101	0.9936	0.0018	0.9480	0.0098	0.9477	0.0101	0.9473	0.0102	6.17
Case 4	0.9023	0.0069	0.9818	0.0018	0.9028	0.0069	0.9023	0.0069	0.9010	0.0073	9.51

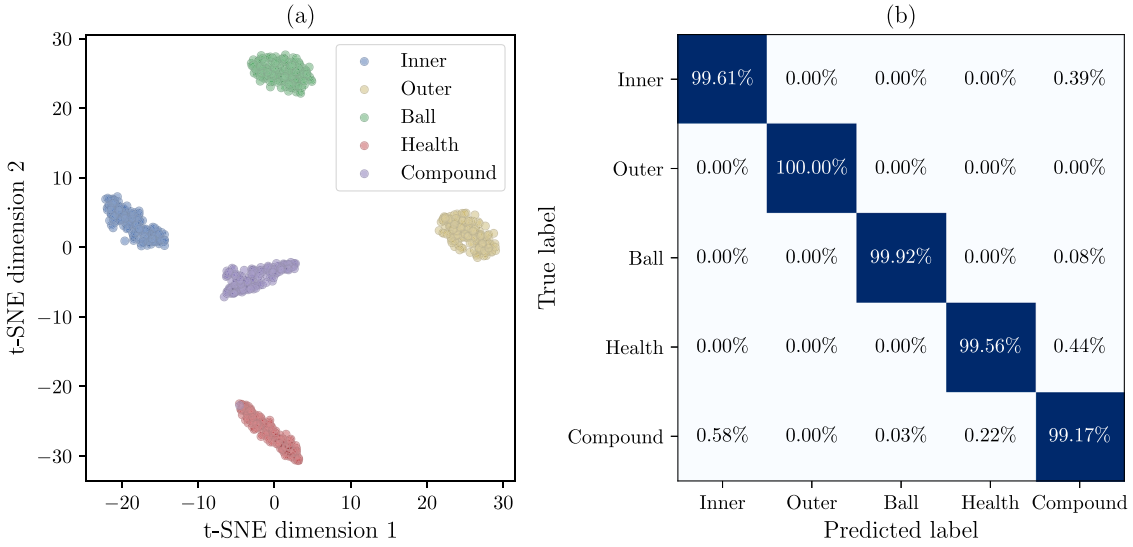

Fig. 16. The multi-fault classification results of the RGSRA-MNN method: (a) t-SNE visualization, (b) average confusion matrix.

parameter transferability, resilience to diverse noise environments, and adaptability to compound fault scenarios, highlighting the method's strong potential for deployment in complex, variable-speed rotating machinery systems.

Despite its promising performance, the current framework also presents certain limitations. Chief among them is the reliance on fully supervised learning, which requires labeled fault data that are often scarce in industrial settings. In addition, the generalizability of the proposed method to novel fault types and diverse operating conditions remains to be thoroughly investigated. Future work will focus on addressing these limitations through semi-supervised learning strategies. Specifically, by leveraging the inherent properties of GSR oscillators — including strong robustness to complex noise and superior parameter transferability — simulated bearing fault signals can be used as labeled data to assist in diagnosing unlabeled real signals. This physics-informed alignment between simulated and real data provides a feasible pathway to reduce reliance on costly labeled samples and enhance the framework's applicability and scalability. Moreover, extending the robust GSR mechanism to support multi-sensor and multi-modal data fusion is expected to further improve its adaptability in heterogeneous industrial environments.

CRediT authorship contribution statement

Xuerui Zhang: Writing – original draft, Validation, Software, Methodology, Investigation, Formal analysis. **Xue Wen:** Writing – review & editing, Methodology. **Lifeng Lin:** Validation, Methodology, Investigation. **Huiqi Wang:** Writing – review & editing, Supervision, Funding acquisition, Conceptualization.

Declaration of competing interest

The authors declare that they have no known competing financial interests or personal relationships that could have appeared to influence the work reported in this paper.

Acknowledgments

This research was partially supported by National Natural Science Foundation of China (Nos. 72071019 and 12226102), Natural Science Foundation of Chongqing, China (No. CSTB2024NSCQ-MSX0551), Natural Science Foundation of Fujian Province, China (No. 2025J011131), and Innovation Fund of Fuzhou University of International Studies and Trade, China (No. FWKQJ2024101). Special thanks are also extended to Dr. Lu Zhang from the School of Mathematics, Sichuan University, China, for her valuable support and contributions to this research.

Appendix A. Derivation of the first-order stochastic asymptotic stability

Since all oscillators in the GSR array are characterized by similar mathematical structures, we will analyze the first-order stochastic asymptotic stability conditions using the kth oscillator for $k = 1, 2, 3, \dots, m$ as an example. For simplicity of notation, the subscript k for all variables (i.e., input signal $s_k(\theta)$, output signal $x_k(\theta)$, and stochastic regulation $\xi_k(\theta)$) and parameters (i.e., $\mathbf{p}_k = [\gamma_k, \omega_k, \sigma_k, \lambda_k, R_k]$, fault order μ_k, amplitude c_k, and phase φ_k) is omitted in the following analysis. The oscillator is expressed as

$$\ddot{x}(\theta) + R\gamma\left[1 + \xi(\theta)\right]\dot{x}(\theta) + R^2\omega^2 x(\theta) = R^2 g(\theta). \tag{A.1}$$

First, take the average of Eq. (A.1), and then, by multiplying both sides of Eq. (A.1) by $\xi(\theta)$ and taking the average, the following expressions can be derived

$$\begin{cases} \langle\ddot{x}(\theta)\rangle + R\gamma\langle\ddot{x}(\theta)\rangle + R\gamma\langle\xi(\theta)\dot{x}(\theta)\rangle + R^2\omega^2\langle x(\theta)\rangle = R^2 s(\theta), \\ \langle\xi(\theta)\ddot{x}(\theta)\rangle + R\gamma\langle\xi(\theta)\dot{x}(\theta)\rangle + R\gamma\sigma^2\langle\dot{x}(\theta)\rangle + R^2\omega^2\langle\xi(\theta)x(\theta)\rangle = 0. \end{cases} \tag{A.2}$$

To decompose the correlations in Eq. (A.2), we use the Shapiro–Loginov formulas:

$$\begin{cases} \frac{\mathrm{d}}{\mathrm{d}t}\langle\xi(\theta)x(\theta)\rangle = \langle\xi(\theta)\dot{x}(\theta)\rangle - R\lambda\langle\xi(\theta)x(\theta)\rangle, \\ \frac{\mathrm{d}}{\mathrm{d}\theta}\langle\xi(\theta)\dot{x}(\theta)\rangle = \langle\xi(\theta)\ddot{x}(\theta)\rangle - R\lambda\langle\xi(\theta)\dot{x}(\theta)\rangle, \end{cases} \tag{A.3}$$

combining Eqs. (A.2) and (A.3), and taking the Laplace transform, we obtain

$$\begin{cases} (s^2 + R\gamma s + R^2\omega^2)X_1(s) + R\gamma X_3(s) = R^2\mathcal{L}[s(\theta)] + (s + R\gamma)x_1(0) + \dot{x}_1(0), \\ R\gamma\sigma^2 s X_1(s) + R^2\omega^2 X_2(s) + R\gamma X_3(s) + X_4(s) = R\gamma\sigma^2 x_1(0), \\ sX_2(s) = X_3(s) - R\lambda X_2(s) + x_2(0), \\ sX_3(s) = X_4(s) - R\lambda X_3(s) + x_3(0), \end{cases} \tag{A.4}$$

where $X_i(s) = \mathcal{L}[x_i(\theta)](s) = \int_0^{+\infty} x_i(\theta)\mathrm{e}^{-s\theta}d\theta$, $i = 1, 2, 3, 4$ are the Laplace transforms of the new defined variables $x_1(\theta) = \langle x(\theta)\rangle$, $x_2(\theta) = \langle\xi(\theta)x(\theta)\rangle$, $x_3(\theta) = \langle\xi(\theta)\dot{x}(\theta)\rangle$, $x_4(\theta) = \langle\xi(\theta)\ddot{x}(\theta)\rangle$; $x_1(0)$, $\dot{x}_1(0)$, $x_2(0)$ and $x_3(0)$ are the initial conditions, whose influences will vanish in the long-time limit $\theta \to \infty$. Thus, the solution of Eq. can be easily obtained and in particular has the following representation:

$$\begin{cases} X_1(s) = R^2 H_1(s)\mathcal{L}[s(\theta)], \\ X_2(s) = R^2 H_2(s)\mathcal{L}[s(\theta)], \\ H_1(s) = \frac{1}{D(s)}\left[(s + R\lambda)^2 + R\gamma(s + R\lambda) + R^2\omega^2\right], \\ H_2(s) = \frac{1}{D(s)}\gamma\sigma^2 Rs, \\ D(s) = (R^2\omega^2 + s^2 + R\gamma s)\left[(s + R\lambda)^2 + R\gamma(s + R\lambda) + R^2\omega^2\right] - s\sigma^2 R^2\gamma^2(s + R\lambda). \end{cases} \tag{A.5}$$

Based on Routh–Hurwitz criterion, we obtain the following first-order stochastic asymptotic stability condition:

$$\begin{cases} d_1 d_4 < d_2 d_3, \\ d_0 d_3^2 < d_1 d_2 d_3 - d_1^2 d_4, \end{cases} \tag{A.6}$$

with

$$\begin{cases} d_0 = R^4\omega^2(\lambda^2 + \lambda\gamma + \omega^2), \\ d_1 = R^3(\lambda + \gamma)(\lambda\gamma + 2\omega^2) - R^3\gamma^2\lambda\sigma^2, \\ d_2 = R^2\gamma^2(1 - \sigma^2) + R^2(\lambda^2 + 2\omega^2) + 3R^2\lambda\gamma, \\ d_3 = 2R(\lambda + \gamma), \end{cases} \tag{A.7}$$

By simplifying the first inequality in Eq. (A.6), we obtain the following expression:

$$\sigma^2 < 1 + \frac{1}{\gamma^2(\lambda+2\gamma)}[\lambda^2(2\lambda+\gamma) + \lambda\gamma(5\lambda+3\gamma) + 2\lambda\omega^2], \tag{A.8}$$

which means Eq. (A.8) holds for all $\sigma \in (0,1)$. Meanwhile, we can reformulate the second inequality as follows:

$$b_1\sigma^4 + b_2\sigma^2 + b_3 > 0, \tag{A.9}$$

where

$$\begin{cases} b_1 = R^6\gamma^4(2\lambda+\gamma), \\ b_2 = -2R^6\gamma^2[2\omega^2(\lambda^2+\gamma^2) + 2\lambda\gamma(\lambda^2+\gamma^2)\lambda^3(2\gamma+\lambda) + 5\gamma^2\lambda^2 + 4\lambda\omega^2], \\ b_3 = R^6[\gamma^2\lambda(2\gamma^2+7\lambda^2) + 9\gamma\lambda^2(\gamma^2+1) + 4\omega^2(2\lambda^3+\gamma^3) + 4\gamma\lambda\omega^2(5\lambda+4\gamma)]. \end{cases} \tag{A.10}$$

Given that all system parameters are strictly positive, which implies that the quartic polynomial coefficient satisfies $b_1 > 0$. Consider the function:

$$f(\sigma^2) = b_1\sigma^4 + b_2\sigma^2 + b_3, \text{ for } \sigma \in (0,1), \tag{A.11}$$

whose first derivative is $\dot{f}(\sigma^2) = 2b_1\sigma^2 + b_2$. Through analysis of parameter sign relationships, we rigorously prove that $\dot{f}(\sigma^2) < 0$ holds for all $\sigma \in (0,1)$, establishing strict monotonic decrease of $f(\sigma)$ over the interval. We further verify that $f(\sigma^2) > 0$ holds in the limits $\sigma \to 0^+$ and $\sigma \to 1^-$. By the continuity theorem and monotonicity, $f(\sigma^2) > 0$ holds for all $\sigma \in (0,1)$. Combined with Eq. (A.9), this result directly proves that the first-moment's asymptotic stability condition in Eq. (A.6) is satisfied for all $\sigma \in (0,1)$.

Based on linear response theory [8,69,70], inverse Laplace transform is used to obtain the long time limit of the first moment $\langle x(\theta)\rangle_{\text{as}}$ and $\langle \xi(\theta)x(\theta)\rangle_{\text{as}}$ in the follow form:

$$\begin{cases} \langle x(\theta)\rangle_{\text{as}} = \langle x(\theta)\rangle|_{\theta\to\infty} = A\sin(2\pi\mu\theta + \psi), \\ \langle \xi(\theta)x(\theta)\rangle_{\text{as}} = \langle \xi(\theta)x(\theta)\rangle|_{\theta\to\infty} = A'\sin(2\pi\mu\theta + \psi'), \end{cases} \tag{A.12}$$

with the output amplitude and phase shift:

$$\begin{cases} A = cR^2\sqrt{\dfrac{m_1^2+m_2^2}{m_3^2+m_4^2}}, \\ A' = c\gamma\sigma^2R^3\sqrt{\dfrac{4\pi^2\mu^2}{m_3^2+m_4^2}}, \\ \psi = \arctan\left(\dfrac{m_2m_3 - m_1m_4}{m_1m_3 + m_2m_4}\right) + \varphi, \\ \psi' = \arctan\left(\dfrac{m_3}{m_4}\right) + \varphi, \end{cases} \tag{A.13}$$

the related coefficients can be expressed as

$$\begin{cases} m_1 = -4\pi^2\mu^2 + R^2\lambda^2 + R^2\gamma\lambda + R^2\omega^2, \\ m_2 = 2\pi\mu(2\lambda+\gamma)R, \\ m_3 = 4\pi^2\mu^2R^2\gamma^2\sigma^2 - \left(4\pi^2\mu^2 - R^2\omega^2\right)\left(R^2\lambda^2 + R^2\gamma\lambda + R^2\omega^2 - 4\pi^2\mu^2\right) - 4\pi^2\mu^2\gamma(2\lambda+\gamma)R^2, \\ m_4 = 2\pi\mu R\gamma\left(R^2\lambda^2 + R^2\gamma\lambda + R^2\omega^2 - 4\pi^2\mu^2\right) - 2\pi\mu\left(4\pi^2\mu^2 - R^2\omega^2\right)(2\lambda+\gamma)R - 2\pi\mu R^3\lambda\gamma^2\sigma^2. \end{cases} \tag{A.14}$$

Appendix B. Derivation of the second-order stochastic asymptotic stability

Next, we derive the second-order stochastic asymptotic stability conditions to ensure the asymptotic stability of the system's second moment $\langle x^2(\theta)\rangle$ for Eq. (A.1), which is crucial for maintaining the reliability of fault detection by preventing random disturbances from overwhelming weak fault characteristics. Denoting $p_1 = x^2(\theta)$, $p_2 = x(\theta)\dot{x}(\theta)$, $p_3 = \dot{x}^2(\theta)$, and differentiating the three equations:

$$\begin{cases} \dot{p}_1 = 2p_2, \\ \dot{p}_2 = -R^2\omega^2p_1 - R\gamma(1+\xi(\theta))p_2 + p_3 + R^3g(\theta)x(\theta), \\ \dot{p}_3 = -2R^2\omega^2p_2 - 2R\gamma(1+\xi(\theta))p_3 + 2R^2g(\theta)\dot{x}(\theta). \end{cases} \tag{B.1}$$

Multiplying Eq. (B.1) by $\xi(\theta)$ and averaging them, we can obtain a linear system for six variables $g_1 = \langle p_1\rangle$, $g_2 = \langle p_2\rangle$, $g_3 = \langle p_3\rangle$, $g_4 = \langle \xi(\theta)p_1\rangle$, $g_5 = \langle \xi(\theta)p_2\rangle$, $g_6 = \langle \xi(\theta)p_3\rangle$:

$$\dot{\mathbf{G}}(\theta) + \mathbf{P}\mathbf{G}(\theta) = \mathbf{F}, \tag{B.2}$$

where

$$\mathbf{G}=\begin{pmatrix} g_1 \\ g_2 \\ g_3 \\ g_4 \\ g_5 \\ g_6 \end{pmatrix},\ \mathbf{P}=\begin{pmatrix} 0 & -2 & 0 & 0 & 0 & 0 \\ R^2\omega^2 & R\gamma & -1 & 0 & R\gamma & 0 \\ 0 & 2R^2\omega^2 & 2R\gamma & 0 & 0 & 2R\gamma \\ 0 & 0 & 0 & R\lambda & -2 & 0 \\ 0 & R\gamma\sigma^2 & 0 & R^2\omega^2 & R(\lambda+\gamma) & -1 \\ 0 & 0 & 2R\gamma\sigma^2 & 0 & 2R^2\omega^2 & R(\lambda+2\gamma) \end{pmatrix},$$

$$\mathbf{F}=\begin{pmatrix} 0 \\ cAR^2\sin(2\pi\mu\theta+\varphi)\sin(2\pi\mu\theta+\psi) \\ 4\pi\mu cAR^2\sin(2\pi\mu\theta+\varphi)\cos(2\pi\mu\theta+\psi) \\ 0 \\ cA'\sin(2\pi\mu\theta+\varphi)\sin(2\pi\mu\theta+\psi') \\ 2cA'R^2\sin(2\pi\mu\theta+\varphi)\left[2\pi\mu\cos(2\pi\mu\theta+\psi')+R\lambda\sin(2\pi\mu\theta+\psi')\right] \end{pmatrix}.$$

Based on Eq. (B.2), the characteristic equation is given by

$$\det(s\mathbf{E}+\mathbf{P})=\begin{vmatrix} s & -2 & 0 & 0 & 0 & 0 \\ R^2\omega^2 & s+R\gamma & -1 & 0 & R\gamma & 0 \\ 0 & 2R^2\omega^2 & s+2R\gamma & 0 & 0 & 2R\gamma \\ 0 & 0 & 0 & s+R\lambda & -2 & 0 \\ 0 & R\gamma\sigma^2 & 0 & R^2\omega^2 & s+R(\lambda+\gamma) & -1 \\ 0 & 0 & 2R\gamma\sigma^2 & 0 & 2R^2\omega^2 & s+R(\lambda+2\gamma) \end{vmatrix}=\sum_{i=0}^{5} q_i s^i + s^6, \tag{B.3}$$

with

$$\begin{cases} q_0 = 8R^6\gamma^2\omega^2(1-\sigma^2)(\gamma\lambda+2\omega^2)+4R^6\gamma^2\lambda^2\omega^2(3-2\sigma^2)+4R^2\lambda\gamma\omega^2(\lambda^2+4\omega^2), \\ q_1 = 4R^5\gamma^4\lambda(\sigma^2-1)^2+2R^3\gamma^3(3\lambda^2+8\omega^2)(1-\sigma^2)+2R^5\gamma^2\lambda(\lambda^2-4\omega^2\sigma^2)+8R^5\gamma\lambda\omega^2(5\gamma+3\lambda) \\ \qquad +16R^5\omega^4(\lambda+2\gamma)+4R^5\lambda^3\omega^2, \\ q_2 = 4R^4\gamma^4(\sigma^2-1)^2+18R^4\gamma^4\lambda(1-\sigma^2)+5R^4\gamma^2\lambda^2(3-\sigma^2)+8R^4\gamma^2\omega^2(5-\sigma^2)+12R^4\lambda\omega^2(\lambda+4\gamma) \\ \qquad +3R^4\gamma\lambda^3+16R^4\omega^4, \\ q_3 = 12R^3\gamma^3(1-\sigma^2)+2R^3\gamma^2\lambda(13-5\sigma^2)+R^3(16\omega^2+\lambda^2)(2\lambda+\gamma)+10R^3\lambda^2\gamma, \\ q_4 = -5R^2\gamma^2\sigma^2+13R^2\gamma^2+15R^2\gamma\lambda+3R^2\lambda^2+8R^2\omega^2, \\ q_5 = 3R(\lambda+2\gamma). \end{cases} \tag{B.4}$$

Using the Routh–Hurwitz criterion, the asymptotic stability condition for the second moment is as follows:

$$\begin{cases} q_i>0,\ i=0,5, \quad q_4q_5-q_3>0, \\ q_3q_4q_5-q_3^2-q_2q_5^2+q_1q_5>0, \\ \dfrac{q_2q_5-q_1}{q_4q_5-q_3}>\dfrac{q_1q_4q_5-q_1q_3-q_0q_5^2}{q_3q_4q_5-q_3^2-q_2q_5^2+q_1q_5}, \\ \dfrac{q_2q_5-q_1}{q_0q_5}-\dfrac{(q_1q_4q_5-q_1q_3-q_0q_5^2)(q_4q_5-q_3)}{(q_0q_5)(q_3q_4q_5-q_3^2-q_2q_5^2+q_1q_5)}>\dfrac{q_3q_4q_5-q_3^2-q_2q_5^2+q_1q_5}{q_1q_4q_5-q_1q_3-q_0q_5^2}. \end{cases} \tag{B.5}$$

Data availability

All datasets used in this study are publicly available at https://data.mendeley.com/datasets/v43hmbwxpm/2.

References

[1] R.B. Randall, J. Antoni, Rolling element bearing diagnostics—A tutorial, Mech. Syst. Signal Process. 25 (2) (2011) 485–520.

[2] A.K. Jardine, D. Lin, D. Banjevic, A review on machinery diagnostics and prognostics implementing condition-based maintenance, Mech. Syst. Signal Process. 20 (7) (2006) 1483–1510.

[3] Z. Wang, Y. Guo, W. Kang, X. Chen, A novel fault feature extraction method for planet-bearing based on generalized total variation model, IEEE Sens. J. 25 (11) (2025) 20870–20879.

[4] C. James Li, J. Ma, Wavelet decomposition of vibrations for detection of bearing-localized defects, NDT & E Int. 30 (3) (1997) 143–149.

[5] D. Yu, J. Cheng, Y. Yang, Application of EMD method and Hilbert spectrum to the fault diagnosis of roller bearings, Mech. Syst. Signal Process. 19 (2) (2005) 259–270.

[6] Y. Hu, W. Bao, X. Tu, F. Li, K. Li, An adaptive spectral kurtosis method and its application to fault detection of rolling element bearings, IEEE Trans. Instrum. Meas. 69 (3) (2020) 739–750.

[7] P. Jun, Z. Fengxing, M. Zhihua, Z. Bing, Rolling bearing fault diagnosis study based on chaos and fractal theory, in: 2010 International Conference on Mechanic Automation and Control Engineering, 2010, pp. 5295–5297.

[8] L. Gammaitoni, P. Hänggi, P. Jung, F. Marchesoni, Stochastic resonance, Rev. Modern Phys. 70 (1998) 223–287.
[9] R. Kozma, W.J. Freeman, Chaotic resonance-methods and applications for robust classification of noisy and variable patterns, Int. J. Bifurc. Chaos 11 (06) (2001) 1607–1629.
[10] C. Palenzuela, R. Toral, C.R. Mirasso, O. Calvo, J.D. Gunton, Coherence resonance in chaotic systems, Europhys. Lett. 56 (3) (2001) 347.
[11] J. Cantisán, M. Coccolo, J.M. Seoane, M.A.F. Sanjuán, Delay-induced resonance in the time-delayed duffing oscillator, Int. J. Bifurc. Chaos 30 (03) (2020) 2030007.
[12] M. Coccolo, B. Zhu, M.A. Sanjuán, J.M. Sanz-Serna, Bogdanov-Takens resonance in time-delayed systems, Nonlinear Dynam. 91 (3) (2018) 1939–1947.
[13] M. Coccolo, J. Cantisán, J.M. Seoane, S. Rajasekar, M.A. Sanjuán, Delay-induced resonance suppresses damping-induced unpredictability, Phil. Trans. R. Soc. A 379 (2192) (2021) 20200232.
[14] Z. Wang, X. Yu, Y. Guo, W. Kang, X. Chen, A noise-enhanced feature extraction method combined with tunable Q-factor wavelet transform and its application to planet-bearing fault diagnosis, Appl. Acoust. 239 (2025) 110845.
[15] Z. Wang, J. Fan, Y. Guo, X. Chen, W. Kang, Research on fault feature extraction for planet-bearing using novel combination operator morphological filtering and stochastic resonance, J. Sound Vib. 607 (2025) 119037.
[16] B. Xu, J. Li, F. Duan, J. Zheng, Effects of colored noise on multi-frequency signal processing via stochastic resonance with tuning system parameters, Chaos Solitons Fractals 16 (1) (2003) 93–106.
[17] Z. Jiang, G. Zhang, Y. Gao, Two-dimensional quad-stable Gaussian potential stochastic resonance model for enhanced bearing fault diagnosis, Appl. Math. Model. 137 (2025) 115657.
[18] Z. Qiao, Y. Lei, N. Li, Applications of stochastic resonance to machinery fault detection: A review and tutorial, Mech. Syst. Signal Process. 122 (2019) 502–536.
[19] J. Yang, S. Rajasekar, M.A. Sanjuán, Vibrational resonance: A review, Phys. Rep. 1067 (2024) 1–62.
[20] A. Rai, S. Upadhyay, A review on signal processing techniques utilized in the fault diagnosis of rolling element bearings, Tribol. Int. 96 (2016) 289–306.
[21] L. He, Z. Jiang, Y. Chen, Unveiling the principles of stochastic resonance and complex potential functions for bearing fault diagnosis, Chaos Solitons Fractals 180 (2024) 114484.
[22] Y. He, Z. Qiao, B. Xie, S. Ning, Z. Li, A. Kumar, Z. Lai, Two-stage benefits of internal and external noise to enhance early fault detection of machinery by exciting fractional SR, Chaos Solitons Fractals 182 (2024) 114749.
[23] V. Berdichevsky, M. Gitterman, Stochastic resonance in linear systems subject to multiplicative and additive noise, Phys. Rev. E 60 (1999) 1494–1499.
[24] S. Burov, M. Gitterman, Noisy oscillator: Random mass and random damping, Phys. Rev. E 94 (2016) 052144.
[25] L. Jiang, L. Lai, T. Yu, M. Luo, Collective stochastic resonance behaviors of two coupled harmonic oscillators driven by dichotomous fluctuating frequency, Chin. Phys. B 30 (6) (2021) 060502.
[26] L. Zhang, L. Lai, H. Peng, Z. Tu, S. Zhong, Stochastic and superharmonic stochastic resonances of a confined overdamped harmonic oscillator, Phys. Rev. E 97 (1) (2018) 012147.
[27] K. Chen, Y. Lu, L. Lin, et al., A new dynamical method for bearing fault diagnosis based on optimal regulation of resonant behaviors in a fluctuating-mass-induced linear oscillator, Sensors 21 (3) (2021) 707.
[28] H. Wang, K. Chen, L. Lin, Bearing fault diagnosis based on the active energy conversion of generalized stochastic resonance in fluctuating-frequency linear oscillator, Meas. Sci. Technol. 32 (12) (2021) 125017.
[29] K. Chen, Y. Lu, R. Zhang, H. Wang, The adaptive bearing fault diagnosis based on optimal regulation of generalized SR behaviors in fluctuating-damping induced harmonic oscillator, Mech. Syst. Signal Process. 189 (2023) 110078.
[30] R. Zhang, K. Chen, H. Wang, The adaptive bearing fault diagnosis based on generalized stochastic resonance in a scale-transformed fractional oscillator driven by unilateral attenuated impulse signal, Meas. Sci. Technol. 34 (1) (2023) 015005.
[31] K. Fyfe, E. Munck, Analysis of computed order tracking, Mech. Syst. Signal Process. 11 (2) (1997) 187–205.
[32] X. Li, J. Yuan, DeepTVAR: Deep learning for a time-varying VAR model with extension to integrated VAR, Int. J. Forecast. 40 (3) (2024) 1123–1133.
[33] Y. Zhou, J. Vuitton, Q. Tian, M. Hecht, Wheel flat detection by using the angular domain synchronous averaging method and axle box acceleration: Simulation and experiment, Measurement 230 (2024) 114508.
[34] J. Yang, C. Yang, X. Zhuang, H. Liu, Z. Wang, Unknown bearing fault diagnosis under time-varying speed conditions and strong noise background, Nonlinear Dynam. 107 (3) (2022) 2177–2193.
[35] Z. Wang, J. Yang, Y. Guo, T. Gong, Z. Shan, Positive role of bifurcation on stochastic resonance and its application in fault diagnosis under time-varying rotational speed, J. Sound Vib. 537 (2022) 117210.
[36] T. Gong, J. Yang, S. Liu, H. Liu, Non-stationary feature extraction by the stochastic response of coupled oscillators and its application in bearing fault diagnosis under variable speed condition, Nonlinear Dynam. 108 (4) (2022) 3839–3857.
[37] R. Randall, J. Antoni, S. Chobsaard, The relationship between spectral correlation and envelope analysis in the diagnostics of bearing faults and other cyclostationary machine signals, Mech. Syst. Signal Process. 15 (5) (2001) 945–962.
[38] D. Han, P. li, S. An, P. Shi, Multi-frequency weak signal detection based on wavelet transform and parameter compensation band-pass multi-stable stochastic resonance, Mech. Syst. Signal Process. 70–71 (2016) 995–1010.
[39] P. Shi, X. Ding, D. Han, Study on multi-frequency weak signal detection method based on stochastic resonance tuning by multi-scale noise, Measurement 47 (2014) 540–546.
[40] Z. Qiao, C. Zhang, C. Zhang, X. Ma, R. Zhu, Z. Lai, S. Zhou, Stochastic resonance array for designing noise-boosted filter banks to enhance weak multi-harmonic fault characteristics of machinery, Appl. Acoust. 236 (2025) 110710.
[41] R. Zhao, R. Yan, Z. Chen, K. Mao, P. Wang, R.X. Gao, Deep learning and its applications to machine health monitoring, Mech. Syst. Signal Process. 115 (2019) 213–237.
[42] D. Hoang, H. Kang, A survey on Deep Learning based bearing fault diagnosis, Neurocomputing 335 (2019) 327–335.
[43] S. Zhang, S. Zhang, B. Wang, T.G. Habetler, Deep learning algorithms for bearing fault diagnostics—A comprehensive review, IEEE Access 8 (2020) 29857–29881.
[44] R. Liu, B. Yang, E. Zio, X. Chen, Artificial intelligence for fault diagnosis of rotating machinery: A review, Mech. Syst. Signal Process. 108 (2018) 33–47.
[45] C. Wang, Z. Qiao, Z. Huang, J. Xu, S. Fang, C. Zhang, J. Liu, R. Zhu, Z. Lai, Research on a bearing fault enhancement diagnosis method with convolutional neural network based on adaptive stochastic resonance, Sensors 22 (22) (2022) 8730.
[46] Y. Guo, J. Zhou, Z. Dong, H. She, W. Xu, Research on bearing fault diagnosis based on novel MRSVD-CWT and improved CNN-LSTM, Meas. Sci. Technol. 35 (9) (2024) 095003.
[47] J. Yao, W. Liang, J. Xiong, Novel intelligent diagnosis method of oil and gas pipeline defects with transfer deep learning and feature fusion, Int. J. Press. Vessels Pip. 200 (2022) 104781.
[48] M. Wang, W. Wang, X. Zhang, H.H.-C. Iu, A new fault diagnosis of rolling bearing based on Markov transition field and CNN, Entropy 24 (6) (2022) 751.
[49] R. Bai, Z. Meng, Q. Xu, F. Fan, Fractional Fourier and time domain recurrence plot fusion combining convolutional neural network for bearing fault diagnosis under variable working conditions, Reliab. Eng. Syst. Saf. 232 (2023) 109076.
[50] Z. Tian, X. Zhang, W. Yan, J. Wang, Bearing fault diagnosis and interpretation based on 2D images and convolutional neural network, in: 2023 Asia Pacific Signal and Information Processing Association Annual Summit and Conference, APSIPA ASC, 2023, pp. 2155–2162.

[51] P. Liu, S. Zhao, L. Kang, Y. Yin, CNN Intelligent diagnosis method for bearing incipient faint faults based on adaptive stochastic resonance-wave peak cross correlation sliding sampling, Digit. Signal Process. 156 (2025) 104871.
[52] A.A. Valido, M. Coccolo, M.A.F. Sanjuán, Time-delayed Duffing oscillator in an active bath, Phys. Rev. E 108 (2023) 064205.
[53] R. Zhang, K. Chen, H. Wang, A robust index-guided GSR approach to improve the efficiency of bearing fault diagnosis, Meas. Sci. Technol. 34 (7) (2023) 075003.
[54] K. Chen, R. Zhang, L. Meng, X. Zheng, K. Wang, H. Wang, The fast bearing diagnosis based on adaptive GSR of fault feature amplification in scale-transformed fractional oscillator, ISA Trans. 157 (2025) 124–141.
[55] D. Huang, J. Yang, J. Zhang, et al., An improved adaptive stochastic resonance method for improving the efficiency of bearing faults diagnosis, Proc. Inst. Mech. Eng. Part C: J. Mech. Eng. Sci. 232 (13) (2018) 2352–2368.
[56] Q. Ma, D. Huang, J. Yang, Adaptive stochastic resonance in second-order system with general scale transformation for weak feature extraction and its application in bearing fault diagnosis, Fluct. Noise Lett. 17 (1) (2018) 1850009.
[57] A. Ortiz, J. Yang, M. Coccolo, J.M. Seoane, M.A. Sanjuán, Fractional damping enhances chaos in the nonlinear Helmholtz oscillator, Nonlinear Dynam. 102 (4) (2020) 2323–2337.
[58] M. Coccolo, J.M. Seoane, S. Lenci, M.A. Sanjuán, Fractional damping effects on the transient dynamics of the Duffing oscillator, Commun. Nonlinear Sci. Numer. Simul. 117 (2023) 106959.
[59] M. Coccolo, J.M. Seoane, M.A. Sanjuán, Fractional damping induces resonant behavior in the Duffing oscillator, Commun. Nonlinear Sci. Numer. Simul. 133 (2024) 107965.
[60] M. Gitterman, Harmonic oscillator with fluctuating damping parameter, Phys. Rev. E 69 (2004) 041101.
[61] C.-T. Chen, Linear System Theory and Design, Saunders college publishing, 1984.
[62] L. Lai, L. Zhang, T. Yu, Collective behaviors in globally coupled harmonic oscillators with fluctuating damping coefficient, Nonlinear Dynam. 97 (2019) 2231–2248.
[63] L. Meng, R. Zhang, L. Lin, H. Wang, Synchronization dynamics and collective behaviors of coupled fluctuating-frequency oscillators in complex networks, Nonlinear Dynam. 112 (23) (2024) 21449–21469.
[64] C. Ma, R. Ren, M. Luo, K. Deng, Stochastic resonance in an overdamped oscillator with frequency and input signal fluctuation, Nonlinear Dynam. 110 (2) (2022) 1223–1232.
[65] X. Chen, Y. Zhang, Y. Su, Y. Zhou, W. Gong, A short time series rolling bearing fault diagnosis method based on FMTF-CNN, Eng. Res. Express 6 (2) (2024) 025346.
[66] J. Sun, X. Wu, V. Palade, W. Fang, C.-H. Lai, W. Xu, Convergence analysis and improvements of quantum-behaved particle swarm optimization, Inform. Sci. 193 (2012) 81–103.
[67] H. Huang, N. Baddour, Bearing vibration data collected under time-varying rotational speed conditions, Data Brief 21 (2018) 1745–1749.
[68] S. Li, H. Wang, C. Yan, Y. Hou, L. Wu, A systematic review of diagnosis methods for rolling bearing compound faults: research status, challenges, and future prospects, Meas. Sci. Technol. 36 (1) (2024) 012008.
[69] M. Dykman, D. Luchinsky, R. Mannella, P. McClintock, N. Stein, N. Stocks, Stochastic resonance: Linear response and giant nonlinearity, J. Stat. Phys. 70 (1993) 463–478.
[70] J. Casado-Pascual, C. Denk, J. Gómez-Ordóñez, M. Morillo, P. Hänggi, Gain in stochastic resonance: Precise numerics versus linear response theory beyond the two-mode approximation, Phys. Rev. E 67 (2003) 036109.